UCRL-8198
Cpy. 2

UNIVERSITY OF CALIFORNIA

Ernest O. Lawrence Radiation Laboratory

TWO-WEEK LOAN COPY

This is a Library Circulating Copy which may be borrowed for two weeks. For a personal retention copy, call Tech. Info. Division, Ext. 5545

BERKELEY, CALIFORNIA

DISCLAIMER

This document was prepared as an account of work sponsored by the United States Government. While this document is believed to contain correct information, neither the United States Government nor any agency thereof, nor the Regents of the University of California, nor any of their employees, makes any warranty, express or implied, or assumes any legal responsibility for the accuracy, completeness, or usefulness of any information, apparatus, product, or process disclosed, or represents that its use would not infringe privately owned rights. Reference herein to any specific commercial product, process, or service by its trade name, trademark, manufacturer, or otherwise, does not necessarily constitute or imply its endorsement, recommendation, or favoring by the United States Government or any agency thereof, or the Regents of the University of California. The views and opinions of authors expressed herein do not necessarily state or reflect those of the United States Government or any agency thereof or the Regents of the University of California.

HANDBOOK OF RADIATION DOSIMETRY

Chapter 14

Heavy Charged-Particle Beams

(Editors: G. J. Hine and G. L. Brownell)
Academic Press, Inc., New York

by

Ann C. Birge, Hal O. Anger, and Cornelius A. Tobias*

Donner Laboratory of Biophysics and Medical Physics
University of California
Berkeley, California

*This communication contains some original data, previously unpublished. The authors' work was supported by a contract between the AEC and the University of California, and by the State of California Cancer Fund.

Chapter 14

HEAVY CHARGED-PARTICLE BEAMS

Ann C. Birge, Hal O. Anger, and Cornelius A. Tobias

I. Introduction 4

II. Physical Properties of Heavy Charged Particles 5

A. Energy Loss 5

B. Relative Stopping Powers 7

1. Stopping Power of Elements 7

2. Stopping Power of Compounds 8

C. Specific Ionization 10

D. Elastic Scattering 11

E. Inelastic Scattering 13

F. The Range-Energy Relation 14

G. Straggling and the Number-Distance Curve 14

H. The Bragg Ionization Curve 17

III. Dose Measurement 19

A. Ionization Chambers 20

1. Types of Ionization Chambers 20

2. Dose Calculation 21

3. Sources of Error 22

B. Faraday Cups 26

1. Construction of a Faraday Cup 26

2. Calculation of Dose and Related Quantities 26

3. Sources of Error 29

C. Particle Counters 30

D. Activation Dosimetry 31

1. The Decay Curve 31

2. Dose Calculation 31

3. Applications 33

E. Photographic Film 34
F. Crystal Detectors 36

IV. Applications 37

Bibliography 40

I. Introduction

In contrast with the very extensive utilization of x-rays, γ-rays, and electrons in medical radiology and radiobiology, the use of heavy particles has been limited to a few isolated groups of investigators. Heavy particles have many potential applications to biology and medicine, however, since they have physical properties that permit the use of improved techniques in radiotherapy and they provide unique experimental conditions for radiobiological studies.

Two main reasons for interest in the biological application of heavy particles lie in their scattering properties and in the ionization pattern of their tracks. Since protons are some 2000 times as heavy as electrons, the angle of scattering in a given collision is reduced by about the same ratio. Hence heavy particles generally produce a more sharply defined beam than electrons of comparable velocity, and undesirable side scattering can be reduced to a minimum. Absorption of heavy-particle beams and shaping of the radiation field may also be accomplished with greater ease than with x-rays or with γ-rays, since the particles have a definite range of penetration instead of following the exponential absorption law. Heavy particles can produce very dense ionization tracks in tissue; hence, they give biological effects that are in many cases qualitatively and quantitatively different from those produced by electrons, x-rays and γ-rays.

Biological experiments have been performed with protons, deuterons, alpha particles, carbon ions, fission recoils, and heavy cosmic ray primaries. Some of the methods by which the particles have been obtained are listed below. Van de Graaff machines have been used to furnish protons in the energy region of 1 to 10 Mev (90). Small cyclotrons have been used to accelerate protons, deuterons, alpha particles, and carbon ions when penetration of a fraction of a millimeter into biological material is sufficient (56, 61, 62). Frequency-modulated cyclotrons have been used to supply particles which penetrate several inches in soft tissue (72). For high-intensity multiply-charged particles or ions, a linear accelerator, possibly combined with a cyclotron, may be suitable in the future (74). Heavy cosmic-ray primaries have been available for biological experimentation through the use of high-altitude balloon flights (67), while fission fragments and light (Li, He) nuclear recoils have been produced in the animal body by neutrons after incorporation of uranium, lithium, or boron into the tissue of the subject (71, 46, 27).

The usual α-particle source for treating very thin layers of biological material is a thin electroplated film of Po^{210} (91).

II. Physical Properties of Heavy Charged Particles

The actual dose delivered to a complex biological specimen is computed from a knowledge of the interaction of charged particles with the material they traverse. These interactions are reviewed briefly before their application to specific dosimetry problems is considered. (See also Chapter 2, Section IV.) For a more detailed discussion of these basic properties the reader is referred to the excellent reviews on the subject (8, 2).

A. Energy Loss

In its passage through material, an ionizing particle is characterized by the amount of energy it loses per unit length of path traversed. This is called the rate of energy loss, the lineal energy transfer (LET), or the stopping power, and it is dependent on the charge and velocity of the incident particle as well as on the nature of the stopping material.

The average energy loss dE/dx per cm path is given by the well-known relations

$$-\frac{dE}{dx} = \frac{4\pi e^4 z^2}{mv^2} NB , \qquad (1)$$

and

$$B = Z\left\{\ln\frac{2mv^2}{I} - \ln(1-\beta^2) - \beta^2\right\}, \qquad (2)$$

where N is the number of atoms per cubic centimeter of the stopping material, Z is the atomic number of the material, m and e are the mass and charge of the electron, ze is the charge of the incident particle, $\beta = v/c$ (where v is the velocity of the incident particle and c the velocity of light), and I is the average excitation potential for the stopping material and is usually determined empirically. For nonrelativistic energies, $\beta \approx 0$, and the term for B can be simplified to

$$B = Z \ln\frac{2mv^2}{I} . \qquad (2a)$$

The dimensionless term B is called the "stopping number" of the material. Equation 1 for the rate of energy loss is valid only if the velocity

v is high enough, $v \geq \frac{z e^2}{\hbar}$, so that the particle does not pick up electrons in its passage through matter. Here $\hbar$ is Planck's constant divided by 2π. In general, empirical results must be used for velocities corresponding to protons of energy less than a few Mev. At low particle velocities there is no adequate theory for the effects of nuclear collisions and charge pickup. Even at intermediate velocities, corrections for shielding of the inner electrons are important.

The rate of energy loss may be expressed in terms of energy loss per gram per cm^2 of absorbing material. This is called the mass stopping power σ_m, and is just

$$\sigma_m = -\frac{1}{\rho}\frac{dE}{dx}, \tag{3}$$

where ρ is the density of the material. The quantity σ_m is independent of the density of the stopping material, since the number of atoms per cm^3 in Eq. 1 is

$$N = \frac{N_o}{A}\rho, \tag{4}$$

where N_o is Avogadro's number, and A is the atomic weight of the stopping material.

The rate of energy loss may also be expressed as atomic stopping power, σ_A, or stopping power per atom, and as electronic stopping power σ_e, which is frequently given in units of ev cm^2 per electron. In this case,

$$-\frac{dE}{dx} = \sigma_e NZ = \sigma_e \frac{N_o \rho}{A} Z. \tag{5}$$

Theoretical curves for the mass stopping powers of protons in water, nitrogen, aluminum, and argon are given in Fig. 1. (For protons in carbon, aluminum and air see Chapter 2, Table XII.) The values for aluminum are those of Smith, (68) the nitrogen and argon values are from Aron, Hoffman, and Williams (5), and the values for water are those of Rich and Madey.(58) Curves for other absorbers may be found in these references. In these calculations I is assumed to be 17.5 ev for hydrogen and 11.5 Z for other elements. The average excitation potential may actually be a function of particle velocity, and appreciably different from the values assumed here.(2, 49) The resultant corrections to the stopping power, however, are only a few percent for energies above 10 Mev.

From Eq. 1 it can be seen that the ratio of the rates of energy loss by two particles of different charge number, z_1 and z_2, but traveling with the same velocity v through the same material, is

$$\frac{\left(\frac{dE}{dx}\right)_1}{\left(\frac{dE}{dx}\right)_2} = \frac{z_1^2}{z_2^2}, \tag{6}$$

Hence the rate of energy loss of other particles can be inferred from the proton curves by the use of the appropriate z^2 factor in the region of validity of Eq. 1.

B. Relative Stopping Powers

1. Stopping power of elements

It can be seen from Eqs. 1 and 2a that if two particles of the same velocity and charge pass through different materials, their rates of energy loss per atom are proportional to the stopping numbers of the two materials. The relative atomic stopping power S_A is defined by the ratio,

$$S_A = \frac{B_1}{B_2} = \frac{Z_1 (\ln 2\ mv^2 - \ln I_1)}{Z_2 (\ln 2\ mv^2 - \ln I_2)}, \tag{7}$$

where the subscripts refer to the two materials.

The relative electronic stopping power S_e is the ratio of the electronic stopping powers of the two materials.

$$S_e = \frac{\sigma_{e1}}{\sigma_{e2}} = \frac{\frac{B_1}{Z_1}}{\frac{B_2}{Z_2}} = \frac{\ln 2\ mv^2 - \ln I_1}{\ln 2\ mv^2 - \ln I_2} \tag{8}$$

The stopping powers of two substances may be compared independently of their densities by considering the relative mass stopping power, S_m:

$$S_m = \frac{-\left(\frac{1}{\rho}\frac{dE}{dx}\right)_1}{-\left(\frac{1}{\rho}\frac{dE}{dx}\right)_2} = \frac{\frac{B_1}{A_1}}{\frac{B_2}{A_2}} = \frac{Z_1 A_2 (\ln 2\ mv^2 - \ln I_1)}{Z_2 A_1 (\ln 2\ mv^2 - \ln I_2)}. \tag{9}$$

We are comparing here the stopping powers of two different substances for an incident particle of the same charge and velocity. It is evident that the

relative stopping power is a function of this velocity, and its value must be chosen for the particular particle velocity under consideration. For the materials used in Fig. 1 the relative mass stopping power for any proton energy can be obtained by taking the ratio of the rates of energy loss in the two materials at that energy.

2. Stopping power of compounds

According to Bragg's rule of additivity, the stopping power of a compound is obtained by adding up the contributions from the individual atoms that comprise the compound. This method neglects any effects of the electronic binding in the molecular compound. Actually, the average excitation potential of an atom may be changed by several percent when it is bound in a molecule. Because this excitation potential appears in a logarithmic term in Eq. 2, however, the resultant change in the stopping power of the compound is small. Careful experiments by Thompson (70) indicate that the largest effects of molecular binding occur in hydrogen, as predicted by theory. His maximum observed deviation from the additivity rule was 2%, and it decreased rapidly with increasing atomic number. Since in biological material only a small fraction of the energy loss is due to hydrogen, and the stopping powers are known only to an accuracy of a few percent, the small deviations from the additivity rule are not significant. Even at low energies, recent measurements with water (22) show agreement within a few percent with the stopping power calculated by the additivity rule.

Some question has been raised whether the stopping power of water is different for the vapor, liquid, and solid states. (55) Recent work indicates no change, within the experimental error.(24, 25) We are not considering here the density effect that begins at relativistic energies.(8)

If a_i is the fraction by weight of the ith element in the compound, and N_i is the number of atoms of the ith element per cm^3 of the compound, then

$$N_i = \frac{N_o \, a_i \, \rho}{A_i} , \tag{10}$$

where A_i is the atomic weight of the ith element, N_o is Avogadro's number, and ρ is the density of the compound. Then Bragg's additivity rule states that

$$- \frac{dE}{dx} = \frac{4 \pi e^4 z^2}{mv^2} \, . \, N_o \, \rho \, \Sigma_i \frac{a_i}{A_i} B_i \, . \tag{11}$$

If we consider the relative mass stopping power of a compound compared to a standard substance,

$$S_m = \frac{-\left(\frac{1}{\rho}\frac{dE}{dx}\right)_{compound}}{-\left(\frac{1}{\rho}\frac{dE}{dx}\right)_{standard}} = \frac{\Sigma_i \frac{a_i}{A_i} B_i}{\frac{B\ standard}{A\ standard}}, \tag{12}$$

or

$$S_m = \Sigma_i\, a_i\, S_{m_i}, \tag{13}$$

where S_{m_i} is the relative mass stopping power of the ith element compared to the same standard substance.

By using Eqs. 5, 9, and 10, we can obtain the relative mass stopping power of the compound from the relative electronic stopping powers S_{e_i} of the elements in the compound, and

$$S_m = \frac{\Sigma_i \frac{a_i\, \sigma_{ei}\, Z_i}{A_i}}{\left(\frac{\sigma_e Z}{A}\right)\ standard} = \frac{\Sigma_i \frac{a_i\, S_{e_i}\, Z_i}{A_i}}{\left(\frac{Z}{A}\right)\ standard}\ . \tag{14}$$

The same result is obtained by using in Eqs. 1 and 2 an effective atomic number Z_{eff} and effective excitation potential I_{eff}, where

$$\ln I_{eff} = \frac{\Sigma_i N_i Z_i \ln I_i}{N Z_{eff}} \tag{15}$$

and

$$N Z_{eff} = \Sigma_i N_i Z_i\ . \tag{16}$$

Calculations based on the composition given by Lea (47) for soft tissue (10% hydrogen, 12% carbon, 4% nitrogen, 73% oxygen, 0.1% sodium, 0.04% magnesium, 0.2% phosphorus, 0.2% sulfur, 0.1% chlorine, 0.35% potassium, 0.01% calcium) give an effective excitation potential, I_{eff}, for tissue of 66.2 ev (48) almost equal to that of water, which is 66.0 ev (58). The effective number of electrons per gram of tissue, however, is 1% less than for water. Hence at all particle energies the curve for water in Fig. 1 can be used for Lea's tissue by subtracting 1%. The computed relative mass stopping power of tissue compared to nitrogen is shown in Fig. 2.

C. Specific Ionization

The specific ionization of a particle is defined as the number of ion pairs formed in a gas per unit track length. It is related to the rate of energy loss or stopping power of the gas by the constant W, which is the average energy expended per ion pair formed:

$$\text{specific ionization} = \frac{dE}{dx}/W \; . \qquad (17)$$

The value of W is not very different for different gases, but it is an important constant, since any dose determination made from ionization-chamber measurements is directly dependent on the value. The review by Binks (9) shows the inconsistencies in experimental determinations of W made up to 1953, but recent results show greater consistency (44). For the noble gases and hydrogen, W is independent of the velocity of the incident particle (41). In all these gases except argon, however, its value may be changed drastically by the presence of small amounts of common impurities (42). In fact, the addition of a suitably chosen impurity to any gas will increase the number of ion pairs formed for the same energy transfer, and hence will lower the apparent value of W, if the ionization potential of the impurity gas lies below the lowest metastable state of the original gas (43). Argon has usually given consistent values of W (26.4 ev per ion pair--See Fig. 3) with only moderate purification because the energy of its lowest metastable state lies below the ionization potentials of the common impurities such as oxygen and nitrogen (17, 43).

The value of W in air, nitrogen, oxygen, carbon dioxide, and various hydrocarbons is found to increase with decreasing particle velocity, for velocities corresponding to protons below 2 Mev (34, 45). Above the velocity of 2-Mev protons the value of W for heavy particles appears to be the same as that for fast electrons, i.e., 34.0 ev per ion pair in air, and 34.9 ev per ion pair in nitrogen (6, 44, 45, 54, 84), although there is still not complete agreement on the value of W in air (7). For lower velocities, the values calculated by Gray (34) for air are given in Fig. 3. Here W for nitrogen is plotted using Gray's correction factor for air. It is advantageous that in this group of gases extreme purification is not so important as in the noble gases and hydrogen. For values of W in many different gases the reader is referred to Jesse and Sadauskis (45).

D. Elastic Scattering

An initially monoenergetic and parallel beam of particles is modified as it passes through an absorbing material because of elastic and inelastic scattering of the particles by the absorbing nuclei. First, the beam gradually increases in width and the particle trajectories do not stay exactly parallel. This is primarily due to numerous elastic collisions involving small angles of deflection. Second, the number of particles in the beam gradually decreases as particles are absorbed and scattered out of the beam by large angles of deflection. This is caused predominantly by inelastic scattering (see below). Elastic scattering due to nuclear forces also contributes to these effects (19), but, for charged particles and absorbers heavier than hydrogen, elastic nuclear scattering is less important than either Coulomb scattering or inelastic nuclear scattering.

If the total kinetic energy of the particles participating in the collision remains unchanged in the process, the scattering is called elastic. Elastic scattering due to Coulomb forces can be calculated from the well-known Rutherford equations. Except for rare single collisions involving large angles, Coulomb scattering results in a series of small-angle deflections known as multiple scattering. The elementary theory for multiple scattering treats the case when the absorber is thick enough so that there are many collisions, and thin enough so that there is not appreciable energy loss by the particle (8, 28). In this case the angular distribution of emergent particles is approximately Gaussian, with a mean-square angle of deflection, $\overline{\theta^2}$

$$\overline{\theta^2} = t\rho \frac{8\pi N_o Z(Z+1) z^2 e^4}{A p^2 v^2} \ln \frac{\theta_{max}}{\theta_{min}} . \qquad (18)$$

The distribution of projected angles is also approximately Gaussian, with a mean-square deviation just half that for the spatial distribution. Here t is the thickness of absorber in cm, and p is the momentum of the incident particle. The minimum angle of scattering, θ_{min}, is determined by the shielding of the nucleus by the atomic electrons, whereas the maximum angle θ_{max} differs according to the theory applicable in the particular case. In most instances the log factor lies between 5 and 10. For example, when 100-Mev protons traverse 2 g/cm^2 of aluminum, the root-mean-square angular deflection is 1.4°.

Since vp is proportional to the kinetic energy of the incident particle, the variation of angular deflection for particles passing through equal thicknesses of material in g/cm^2 is roughly

$$\sqrt{\overline{\theta^2}} \sim \frac{z\sqrt{Z}}{vp} \sim \frac{z\sqrt{Z}}{\text{kinetic energy}} \tag{19}$$

and is independent of the mass of the particle. As before, z and Z are atomic numbers of incident and absorbing nuclei, respectively. For the same kinetic energy, a lighter particle has a longer range, and hence undergoes more scattering before the end of its range.

The radial spread of a particle beam in passing through an absorber is also approximately Gaussian, and is closely related to the angular spread. As the beam of particles emerges from an absorber of thickness t cm, the mean-square radial distance $\overline{r^2}$ from the center of the beam is

$$\overline{r^2} = \frac{1}{3}\,\overline{\theta^2}\,t^2\,, \tag{20}$$

where $\sqrt{\overline{\theta^2}}$ is in radians. Note that the radial distribution is dependent on the density of the material. For the same mean-square angle of deflection, the radial spread of the beam increases linearly with the distance traveled. Thus for the same angular distribution, the radial spread is greater for less condensed materials. The factor of 1/3 comes from averaging the contributions to the scattering from all depths of the absorber. If the increase in lateral spread is calculated for the beam after it emerges from an absorber, the factor of 1/3 is omitted. Thus for a beam of 100-Mev protons passing through 2 g/cm^2 of aluminum (t = 0.74 cm), $\sqrt{\overline{r^2}}$ is only 0.01 cm. If the same beam continues in air, however, for 10 cm after emerging from the absorber, the root-mean-square radial spread is 0.25 cm.

Actually the true distribution in angle of the emergent beam is not Gaussian, but has a tail due to less frequent scattering at large angles. For a more accurate theory, single scattering and the intermediate region of plural scattering for only a few collisions must be considered. The problem of multiple scattering in thick absorbers, when appreciable energy is lost by the particles, may be treated by numerical integration.(26) It should also be noted that multiple scattering produces a small but usually negligible range shortening and contributes to range straggling (13).

E. Inelastic Scattering

Some of the accelerated particles do not proceed to the ends of their ranges, but lose their kinetic energy or are scattered out of the beam by inelastic collisions. For example, when 300-Mev protons are stopped in water about one-third of the protons are lost from the beam before the end of their range. When these inelastic collisions occur secondary particles and, at higher energies, nuclear stars are produced which modify the dose and the quality of the radiation.

The cross section for inelastic scattering is negligible for charged particles with insufficient energy to penetrate the Coulomb barrier. In light substances this energy is a few Mev per nucleon. At energies only a little above the threshold value the cross section for inelastic scattering is not easily measured but theory indicates that it will rise to a constant value at higher energies (12). In the energy region between 50 Mev and a few Bev per nucleon the measured total inelastic cross section σ_{inel} is approximately two-thirds the "geometric" area of the absorbing nucleus (20, 53), or

$$\sigma_{inel} \approx \frac{2}{3} \pi R_A^2 . \tag{21}$$

The nuclear radius R_A is given approximately by (19)

$$R_A = A^{1/3}\ 1.4 \times 10^{-13}\ \text{cm} , \tag{22}$$

where A is the atomic number of the absorber.

As an example, consider 300-Mev protons passing through 1 cm of water. In this case approximately 0.9% of the protons are lost because of inelastic collisions with the oxygen nuclei in the water. There are many different reactions that may occur at this energy, but most of the energy of the scattered particles is carried outside the beam by fast nuclear fragments. On the average about 30 Mev remains in each collision as excitation of the residual nucleus (51), and about half of this energy goes into heavily ionizing secondaries. The rest escapes chiefly by means of neutron emission. The dose due to the slow nuclear fragments in the example above turns out to be about 1.7% of the dose due to ionization from the primary beam. Similar calculations indicate that for energies from 0 to 400 Mev the dose contribution from heavy nuclear fragments produced by inelastic scattering does not exceed 2%. The biological effect of heavy recoils may be more important than their dose contribution would indicate, since the heavy recoils may have a very high relative biological effectiveness (23).

F. The Range-Energy Relation

The range of a particle can be found theoretically by integrating the rate of energy loss from the initial energy E_o down to zero energy. In practice, however, this integration cannot be carried down to zero, since Eq. 1 is not valid at very low energies.

From Eqs. 1 and 2, the distance ΔR traveled through an absorber by a particle of mass M and atomic number z for a decrease in energy from E_1 to E_2 is

$$\Delta R_{z,M}(E_1 - E_2) = \int_{E_2}^{E_1} \frac{dE}{-\frac{dE}{dx}} = \frac{M}{Z^2} \frac{m}{4\pi e^4 N} \int_{v_2}^{v_1} F(v) . \qquad (23)$$

Since the value of the integral is dependent only on the velocity of the particle, the ranges of two different particles passing through the same stopping material with the same initial velocities are related by

$$R_1(v) = \frac{M_1}{M_2}\left(\frac{z_2}{z_1}\right)^2 R_2(v) - C . \qquad (24)$$

The constant c, small but not zero, is determined empirically for particles of different charge. It takes into account the capture and loss of electrons at low velocities. For range differences above this region the constant c subtracts out, and a single range-energy relation is sufficient for different particles in each stopping material. Theoretical range-energy curves for protons in water (58), nitrogen (5), aluminum (68), and argon (5), are given in Figs. 4, 5, and 6. These materials are often used in absorbers or ionization chambers. Curves for other materials can be found in the references. For tissue of the composition given by Lea (47) the calculated range is just 1% longer than in water. The theoretical ranges of protons in carbon, aluminum, and air are tabulated in Chapter 2, Table XII.

G. Straggling and The Number-Distance Curve

The theoretical energy-loss equations describe the average energy loss by a particle traversing material. Actually this energy is lost in a finite number of collisions, and there are fluctuations both in the energy lost per collision and in the number of collisions for individual particles traversing a given amount of absorber. Hence, there are fluctuations in the total ranges of particles of the same initial energy.

To a first approximation the ranges of the particles of initial energy E_o are distributed in a normal or Gaussian fashion about the mean range R_o. The fraction of particles with ranges between R and R + dR is then

$$p(R)\,dR = \frac{1}{\sqrt{2\pi\,\Delta_R^2}}\,e^{-(R-R_o)^2/2\Delta_R^2}\,dR\,, \tag{25}$$

where Δ_R^2 is the mean square fluctuation in range. For velocities corresponding to protons above a few Mev, the mean-square fluctuation in range is given by the expression (60, 49)

$$\Delta_R^2 = \overline{(R - R_o)^2} = \int_o^{E_o} \frac{4\,\pi\,e^4\,z^2\,NZ}{\left(\frac{dE}{dx}\right)^3}\,\frac{\left(1 - \frac{\beta^2}{2}\right)}{(1 - \beta^2)}\,dE\,. \tag{26}$$

Equations 1 and 26 show that for particles of different masses, M_1 and M_2, but of the same initial velocity, passing through the same material, the straggling parameters Δ_R^2 are related by

$$\frac{\Delta_{R_1}^2}{\Delta_{R_2}^2} = \frac{M_1}{M_2}\,\frac{z_2^4}{z_1^4}\,. \tag{27}$$

If we define the fractional straggling as $\frac{\sqrt{\Delta_R^2}}{R}$, and neglect the constant in Eq. 24, we see that the fractional straggling for particles of the same velocity is independent of charge and varies inversely with the square root of the mass of the particle:

$$\frac{\left(\frac{\sqrt{\Delta_R^2}}{R}\right)_1}{\left(\frac{\sqrt{\Delta_R^2}}{R}\right)_2} = \frac{\sqrt{M_2}}{\sqrt{M_1}}\,. \tag{28}$$

The fractional straggling varies slowly as a function of initial particle velocity, and it is not very different for different materials. Calculations have been made by Symon (60, 69) and by Caldwell (18).

In actual experiments the quantity measured is usually not the differential distribution of particle ranges, but rather the number-distance curve, or integral range curve. This measurement may be made by determining the flux F of particles traversing an absorber as a function of the absorber

thickness x. Figure 7 shows a typical number-distance curve obtained from Faraday-cup measurements with 190-Mev deuterons. For low-energy particles, which are stopped only by energy loss through ionization, the number-distance curve remains constant from zero absorber to a thickness almost equal to the mean range of the particles. At high energies, however, particles are lost from the beam by inelastic scattering, and the number-distance curve has a finite slope $\frac{dF}{dx}$. An estimate of the inelastic scattering cross section σ_i can be obtained from this slope (53). Thus,

$$\sigma_i \sim \frac{1}{NF}\frac{dF}{dx}, \tag{29}$$

where F is the flux of particles, x is the absorber thickness in cm, and N is the number of atoms per cm^3 of the absorber. The mean range R_o of the particles can be obtained from Fig. 7 by considering the final section of the curve, where the distribution in ranges is approximately Gaussian.

For beams of low energy and low intensity, the instrument used to measure the number-distance curve is often an ionization chamber or counter with associated electronic equipment, which is sensitive only to particles with a certain minimum residual range r_1. This range corresponds to the minimum energy that the particle must expend in the measuring instrument in order to be counted. The ionization chamber measures all particles with ranges greater than $x + r_1$, where x is the distance traveled through the absorber. Then

$$P(x) = \int_{x+r_1}^{\infty} p(R)\, dR = \frac{1}{\sqrt{2\pi\,\Delta_R^2}} \int_{x+r_1}^{\infty} e^{-(R-R_o)^2/2\Delta_R^2}\, dR\,. \tag{30}$$

For a group of particles initially homogeneous in energy, Bethe and Ashkin have shown that the shape of the number-distance curve is independent of the value of r_1. The mean range R_o is equal to the value of $x + r_1$ for which half the particles are counted.

Often the quantity measured is the extrapolated number-distance range, R_{ext}, obtained by drawing the tangent to the number-distance curve at the point of steepest slope. Then

$$R_{ext} - R_o = \sqrt{\frac{\pi}{2}\,\Delta_R^2}\,. \tag{31}$$

The above relation is valid only for a Gaussian distribution in ranges. If the initial particle beam has a known inhomogeneity in energy, the shape of the number-distance curve can be calculated. In the special case where the initial energy distribution is approximately Gaussian, the superposition of several Gaussian distributions gives a final Gaussian with mean-square deviation equal to the sum of the individual mean-square deviations. Thus the observed fluctuation in range results from the energy spread of the original beam, the inherent range straggling caused by statistical fluctuations in the energy loss as described by Eq. 26, and the straggling introduced by multiple small angle scattering which causes some particles to travel more circuitous paths than others (Section II D):

$$\Delta^2_{R\ \text{observed}} = \Delta^2_{R\ \text{energy spread}} + \Delta^2_{R\ \text{straggling}} + \Delta^2_{R\ \text{multiple scattering}} \tag{32}$$

In many cases, the inhomogeneity in initial energy of the beam can be estimated by comparing the observed number-distance curve with the curve expected from inherent range straggling. Caution should be used in measurements involving particles in the energy region of 100 Mev and above, however, since their range distribution is not exactly Gaussian (18, 52).

H. The Bragg Ionization Curve

A Bragg curve is a plot of the relative specific ionization of a collimated beam of particles as a function of the thickness of absorber that the beam has traversed. It can be obtained experimentally by taking the ratio of current from two ionization chambers one of which is placed before and the other after a variable absorber, as shown in Fig. 8. A typical Bragg curve for 190-Mev deuterons is shown in Fig. 7. Since the rate of energy loss of a particle increases with decreasing particle velocity until it reaches a maximum near the end of its path, the Bragg curve rises with increasing absorber thickness and reaches a peak near the mean range of the particles. The Bragg curve should be distinguished from the ionization curve for an individual particle. Range straggling due to statistical fluctuations in energy loss as well as to multiple elastic scattering and inelastic scattering at high energies cause the Bragg curve to have a lower and wider peak than the single-particle ionization curve. Since the amount of straggling increases almost linearly with the thickness of absorber, the sharpest peaks are obtained from monoenergetic beams of low energy. As the energy is increased, more absorber is needed to bring the particles to rest, and the effects of straggling are increased.

A Bragg curve can be constructed mathematically from the theoretical range straggling distribution curve and the single-particle ionization curve.

By a comparison of the observed Bragg curve with the calculated one, the initial energy spread of a beam can be estimated (52). The mean range of the particles can also be obtained from the Bragg curve (52, 37), but the point on the curve that corresponds to the mean range is different for beams of different initial energy.

In practice the shape of the observed Bragg curve may also be influenced by the geometry of the collimating equipment, since the beam may contain low-energy particles scattered from the inside surfaces of the collimator. In addition, even if the particle trajectories are initially parallel, scattering in the absorbing material causes the beam to spread as it approaches the end of its range. For the irradiation of small targets it may be necessary to know the relative ionization in the central portion of the beam. Then the collection area of the ionization chamber should be limited to the central area of the beam, and a Bragg curve is observed of slightly different shape from the conventional Bragg curve obtained with a collection area larger than the cross section of the beam.

For an adequate description of the beam in three dimensions a series of isodose surfaces is necessary. Figure 9 shows a typical set of isodose surfaces for a 190-Mev deuteron beam of circular cross section in lucite. The number on each isodose curve gives the dose compared with the surface dose. Methods for obtaining these curves are discussed in Sections ~~IV-A~~. III-D, E and F.

III. Dose Measurement

There are two basic approaches to the problem of measuring the dose delivered to a target by a beam of nuclear particles. The first approach is based on measurement of the energy transferred by the beam to a test body and conversion of this quantity to the energy lost in the target. The second method consists of measurement of the number of particles per unit area in the beam, which, together with the rate of energy loss of each particle, can be used to calculate the total energy lost in the target. Instruments used for the first approach include calorimeters, chemical dosimeters, ionization chambers, photographic film, scintillation detectors, and crystal detectors such as AgCl or CdS. The quantity measured--for instance calories, electric current, optical density, etc.--is converted to energy loss in the test body by a factor appropriate to each instrument. The actual dose to the target is then calculated by multiplying that energy loss by the relative mass stopping power of the target material in comparison with the material of the measuring instrument. Instruments used to determine the number of particles in the beam are Faraday cups, particle counters, and activation dosimeters. The dose is calculated from the number of particles per unit area in the beam and the stopping power of the target material for these particles. Only the methods most frequently used for dosimetry with heavy-particle beams are described here.

The measurement of dose is not complete unless the distribution of dose throughout the target is known. When only a thin layer of material is irradiated, it is necessary to know the beam profile, which is the dose distribution or flux-density distribution in a plane perpendicular to the direction of the beam. In many applications it is necessary to know the dose distribution in three dimensions. This information can be obtained by combining a series of beam profiles taken at different depths in the target or in a phantom of similar absorbing material. The dose distribution may be represented as a series of isodose surfaces, examples of which are given in Figs. 9 and 18. Although in principle almost any method of dose measurement can be used for obtaining isodose surfaces, the choice of technique is usually determined by the conditions of each experiment. Several methods are discussed in the following sections.

Another important factor that must be known in biological studies is the rate of energy loss of the particles or their lineal energy transfer (LET),

since the same dose delivered by particles with different LET values can produce quantitatively and qualitatively different effects (92). If possible, the distribution of LET values at each point in the sample should also be known.

A final factor that should be considered is the microscopic distribution of ionization along the tracks of individual particles. In particular, two particles of different charge and velocity may have the same LET, but the radial spread of ionization produced by their δ-rays is greater for the particle with higher velocity and higher charge. This factor may have biological significance, especially for particles of very high charge number (64).

A. Ionization Chambers

The instrument most often used to measure dose with high-energy beams is an ionization chamber with plane parallel electrodes. Ionization chambers have the advantage that a relatively large current is produced while only a small amount of beam energy is absorbed.

1. Types of Ionization Chambers

An ionization chamber in which the collecting field is parallel to the direction of the beam is shown in Fig. 10. This type of ionization chamber is convenient in size, and the collection volume may be limited to the central part of the beam by making the collection electrode smaller than the beam area. When a sufficiently large guard electrode surrounds the collection electrode, the electric field is uniform and parallel. The collection volume, which must be known for the dose calculation, is then defined by the area of the collection electrode and the depth of the chamber. The electrodes may be thin metal foil, or plastic that is coated with an electrically conducting film, such as DuPont silver paint.

An ionization chamber in which the collection field is perpendicular to the direction of the beam is shown in Fig. 11. This configuration reduces columnar recombination (described later in this section). It also places a minimum of absorbing material in the path of the beam. It has the disadvantage that the beam must be collimated into an area smaller than the dimensions of the ionization chamber in order for the chamber to present a uniform absorbing thickness to the beam. In this case the effective collection volume of the chamber is determined by the cross-sectional area of the beam. An accurate dose calculation is then difficult because of scattering and beam divergence.

Since nuclear-particle beams from accelerators fluctuate in intensity, the current from the ionization chamber is usually integrated in order to determine the total dose delivered. A typical arrangement for integrating small currents is shown in Fig. 13. The charge liberated in the ionization chamber is integrated by the condenser C, and the potential V_c across the condenser is measured with the aid of a vacuum-tube electrometer. It is advantageous to use an electrometer with nearly 100% inverse feedback, so that the collection electrode is always held effectively at ground potential. This reduces the collection of stray ions from regions of the chamber outside the intended sensitive volume and reduces leakage of charge from the collector to ground. It also reduces the effective magnitude of ionization-chamber and cable capacity by the feedback factor.

2. Dose Calculation

If the charge Q (in coulombs) is collected from an ionization chamber located at the point P, the dose D in rads to the target at that point is

$$D = \frac{Q W S_m 10^5}{V \rho} . \qquad (33)$$

Here V is the collection volume of the ionization chamber in cm^3, ρ is the density in g per cm^3 of the ionization chamber gas at the ambient temperature and pressure, W is the energy in ev per ion pair for the gas, and S_m is the relative mass stopping power of the target material compared with the gas. The factor 10^5 comes from conversion of the units of measurement, that is, charge per ion pair to coulombs, and ev per g to rads.

In many applications the dose must be measured by an ionization chamber that is displaced from the target, for example when the target is an organ deep within the body and the ionization chamber is at the surface. The dose received by the target differs from the dose measured at the surface because of divergence of the beam, scattering by intervening material, and the Bragg ionization effect. Then the dose D_P delivered to the target at P can be calculated from the charge Q_M collected from an ionization chamber located at point M near the surface of the subject, by the relation

$$D_P = \frac{Q_M W_M S_{mP} K 10^5}{V_M \rho_M} . \qquad (34)$$

Here S_{mP} is the relative mass stopping power of the target material compared to the ionization-chamber gas for particles with the energy of those at P. Values of S_m for protons in soft tissue compared to nitrogen are given as a function of proton energy in Fig. 2. The average energy of the particles at P can be determined from their initial energy and the amount of intervening absorber by using the range-energy relations in Section II-F. The factor ρ_M is the density of the ionization chamber gas and V_M is its volume, while K is the ratio of the energy loss per gram of gas in an ionization chamber if it were located at P compared to the energy loss in the ionization chamber located at M.

The factor K can be determined experimentally by constructing a phantom of absorbing material equivalent to the subject and measuring the charge collected in two ionization chambers located at M, near the surface of the phantom, and at P, the target point within the phantom. Then K is obtained from the relation

$$K = \frac{Q_P W_P V_M \rho_M}{Q_M W_M V_P \rho_P}, \tag{35}$$

where the subscripts refer to the ionization chambers located at points P and M. The values of W for different gases are discussed in Section II-C. In some gases W varies with the particle velocity, but for velocities which correspond to protons above 2 Mev, W is constant for any gas, and their ratio W_P/W_M is unity.

It is often more practical to determine K from photographic measurements (Section III-E) or by activation dosimetry (Section III-D), especially when detailed information on the dose distribution in three dimensions is needed. On the other hand, where a broad beam is used to irradiate a thin sample, the factor K is the same as the Bragg ratio (Section II-H). The approximation is often made that

$$D_P \approx KD_M, \tag{36}$$

where D_M is the tissue dose at point M calculated from Eq. 33. This neglects the variation of S_m with the energy of the particles, but is often justified for high-energy particles where S_m varies but slowly with energy.

3. Sources of Error

The calculation of dose from ionization-chamber measurements is inherently limited by uncertainties in the values of W and S_m. The values

of these constants as known at the present time are probably accurate within a few per cent. It should be pointed out, however, that small amounts of impurities in the gas may cause the value of W to be lower than the value obtained if the gas is of high purity. (See Section II-C) Some gases are worse than others in this respect. For this reason, and to minimize recombination errors discussed below, dry nitrogen appears to be particularly suitable as an ionization-chamber gas for dosimetry measurements.

Other sources of error include the contribution to ionization by secondary particles, difficulty in determining the sensitive volume of the ionization chamber, and the recombination of positive and negative ions in the gas. Secondary particles include low-energy electron recoils or delta rays knocked out of the walls of the ionization chamber, and nuclear fragments produced in inelastic collisions. Calculations indicate that the contributions from secondaries are less than 2% in thin-walled ionization chambers. This situation is the opposite of that with x-rays, where the ionization is predominantly produced by secondary electrons from the surrounding material. Tobias and Anger showed by two independent tests that the wall effects are small for 190-Mev deuterons (77). First, the ionization produced in the chamber did not change appreciably when the wall material was changed from low Z to high Z. The materials used included graphite-coated polystyrene, and aluminum, copper, and lead. Second, within the experimental error (± 1%) the current produced in the plane parallel chamber was proportional to the distance between the high-voltage and collection electrodes.

Another source of error is uncertainty in the sensitive volume of the ionization chamber due to distortion of the collection field by neighboring ground planes. This source of error can be minimized by making the guard electrode as large as possible. An additional error may be introduced if the electrodes are thin foils that are deformed by the electric field. In this case the sensitive volume may vary with the collection voltage, owing to bending of the foils. Another source of error arises from ions collected on the back of the collection electrode. This error is eliminated if a double chamber is constructed with the collection electrode placed between two high-voltage foils.

One of the most serious errors in ionization-chamber measurements results from the recombination of positive and negative ions before they migrate to the high-voltage and collection electrodes. (See Chapter 4, Section

II-B.) The effects of recombination may be observed by plotting a saturation curve of the ionization current for a given beam intensity as a function of the collection voltage. At voltages sufficiently high to collect nearly all the ions produced, the curve reaches a plateau. In general, the rate of recombination of ions is proportional to the density of ions of both signs. If n_+ and n_- are the numbers of positive and negative ions per cm^3,

$$\frac{dn_{\pm}}{dt} = \alpha n_+ n_- , \qquad (37)$$

where α is the coefficient of recombination (50). In practice the problem is complicated because the ions may be formed in dense tracks, the beam may be pulsed, and space charge may modify the electric field. The amount of recombination is reduced by a large factor 10^7 if the negative charge carriers are electrons instead of ions, since the drift velocity of electrons is about 10^3 times as high as that of ions, and their coefficient of recombination is about 10^4 times as small. The negative carriers will be electrons unless they combine with neutral atoms to form negative ions. Hence the best gases for ionization chambers are those with negligible electron attachment, namely the noble gases, hydrogen, nitrogen, CO, and CO_2. Gases and vapors with a high coefficient of electron attachment--such as oxygen, water vapor, acetone, carbon tetrachloride, and the halogens--should be avoided (35, 87). Even small amounts of these gases present as impurities result in the formation of negative ions.

For heavy particles the two main types of recombination are columnar or initial recombination, which occurs within individual tracks and depends on the specific ionization of the particles, and volume or general recombination, which occurs throughout the volume of the chamber and hence depends on the average dose rate. For very densely ionizing particles such as carbon nuclei, fission fragments, or alpha particles near the end of their range, the main type of recombination is columnar. When both positive and negative charge carriers are heavy ions the fractional columnar recombination can be calculated from Jaffe's theory (40). (See Chapter 4, Section II-B-6). When the negative carriers are electrons, however, they diffuse out of the tracks rapidly, and this type of recombination is usually negligible.

After the charge carriers have diffused out of their original configuration, they are still subject to volume recombination until they are

collected. Since for a constant collection voltage the density of positive and negative charges in the chamber is roughly proportional to the rate of ionization of the gas, Eq. 37 shows that the amount of recombination increases with the square of the dose rate. Hence as the dose rate is increased, higher collection voltages are necessary to reach the plateau of the saturation curve, and at very high dose rates the curve may show an appreciable slope in the entire range of practicable voltages.

The problem of recombination is particularly difficult with pulsed beams like those from synchrocyclotrons and linear accelerators, where the instantaneous dose rate may be a million times the average dose rate. Voltage saturation curves in air and nitrogen obtained with 190-Mev deuterons from the Berkeley synchrocyclotron are shown in Fig. 13. The curves were obtained by taking the ratio of charge collected from the ionization chamber to charge collected on a Faraday cup, whose efficiency does not depend on dose rate. (See next section.) At the relatively low average dose rate of 1000 rad per minute, the saturation curve has a slope that approaches zero at the highest voltages. The curves in Fig. 13 were plotted with the assumption that 100% collection was obtained at this low dose rate at the highest collection voltage. Then it is apparent that only 90% of the ions formed were collected at 5000 volts and an average dose rate of 7000 rad per minute. With this type of comparison a correction for recombination can be obtained for an ionization chamber that is not operated under saturation conditions. In this case it is necessary to calibrate the ionization chamber at various dose rates against an instrument whose response is proportional to dose rate. Activation dosimetry (Section III-D) as well as a Faraday cup can be used for this purpose. Data obtained in this way are shown in Fig. 14, where the error due to recombination at a constant collection voltage is shown as a function of the dose rate. (4, 63)

A theoretical discussion of recombination for both continuous (16) and pulsed beams (14, 15) is given in Chapter 4. The experimental saturation curves that have been obtained with heavy-particle beams (77, 11) do not fit the theories very closely, but qualitative agreement confirms the conclusion that for the same electric field a higher fraction of charge is collected for a smaller electrode spacing. Thus the requirements of both saturation and uniform electric field favor chambers with a small electrode spacing.

B. Faraday Cups

A Faraday cup consists of a metal absorbing block, which is sufficiently thick to stop the beam, supported on insulators inside an evacuated chamber. The charge of the beam is transferred to the abosrbing block, and the number of particles in the beam can be calculated from the charge collected. In radiochemical applications (31, 83), where the entire energy of the particles is expended in the target, the target itself may form the Faraday cup. In general, however, the Faraday cup must be placed behind the target, and the dose calculation may be complicated by scattering. In some cases--for instance, studies of molecular structure (56)--the flux density of bombarding particles is the quantity to be determined, but in applications where the energy transfer or dose is to be determined, the Faraday cup is not so convenient to use as an ionization chamber. Furthermore, low doses cannot be measured accurately by a Faraday cup because of the small charge collected. It is a very useful instrument, however, for determining the range and hence the energy of the particles in a beam (Sections II-F and II-G). Since its efficiency does not vary with beam intensity, it can be used to calibrate an ionization chamber at high dose rates, where the response of the ionization chamber may become nonlinear (Section III-A-3).

1. Construction of a Faraday Cup

Depending on the energy of the beam to be measured, the beam-absorbing element may be a relatively thin metal plate, or it may be a thick block. A typical Faraday Cup is shown in Fig. 15. The copper or brass block that stops the beam is supported on blocks of teflon insulating material. A vacuum is maintained around the block by a suitable pump. A thin window is provided in the housing to permit the beam to enter the Faraday cup even when the beam energy has been reduced to a low value by passing through absorbing material. The current obtained from a high-energy proton beam which delivers 1000 rad per minute is on the order of 10^{-11} ampere per cm^2. This current can be integrated and measured with a condenser and electrometer such as the type shown in Fig. 12.

2. Calculation of Dose and Related Quantities

If the beam current I_F in amperes is collected on a Faraday cup, the flux F of particles per sec is given by the relation

$$F = \frac{I_F c}{ze \cdot 10} = \frac{I_F 10^{19}}{z\, 1.602} \quad . \tag{40}$$

where 10 ze/c is the charge on each particle in coulombs. Here z is the atomic number of the particle, e is the charge of the electron in electrostatic units, and c is the velocity of light in cm/sec. The total number n of particles collected on the cup in time t is related to the total charge Q_F in coulombs collected on the cup by

$$n = \int_0^t F dt = \frac{Q_F c}{ze\, 10} = \frac{Q_F 10^{19}}{z\, 1.602} \quad . \tag{41}$$

In radiochemical applications, where the target itself forms the Faraday cup and the entire energy E_o (in Mev) of the particles is expended in the target, the total energy transfer U or integral dose in Mev is just nE_o, or

$$U = \frac{Q_F E_o 10^{19}}{z\, 1.602} \quad . \tag{42}$$

Often the quantity of interest is not the total flux F of particles/sec, but the flux density f in particles/cm^2-sec. It is this quantity that is related to the dose. To determine the flux density at any point from the total flux it is necessary to know the profile of the beam, since the beam is seldom of uniform intensity over its entire area.

If i_F is the current density in amperes/cm^2 collected on the Faraday cup, $i_F = \frac{dI_F}{da}$, and

$$f = \frac{i_F}{z} \frac{10^{19}}{1.602} \quad . \tag{43}$$

The density of particles per cm^2 $\frac{dn}{da}$ is then the flux density integrated over time t, and

$$\frac{dn}{da} = \int_0^t f dt = \frac{q_F}{z} \frac{10^{19}}{1.602} \quad , \tag{44}$$

where q_F is the charge density collected on the cup in coulombs/cm^2. If D is the dose in rads,

$$D = \frac{dn}{da} \sigma_m \frac{e}{c} \cdot 10^{12} = \frac{q_F}{z} \sigma_m \cdot 10^{11} \quad . \tag{45}$$

Here σ_m is the mass stopping power of the target material in Mev g^{-1} cm^2 for the beam particles at the energy they have when passing through the target (see Fig. 1). The factor of 10^{11} comes from conversion of units, namely the charge per proton from electrostatic units to coulombs and Mev/g to rads. From Eq. 6, $\sigma_{m,z}$, the mass stopping power for a particle of charge number z, is related to $\sigma_{m,p}$ for a proton of the <u>same velocity</u> by $\sigma_{m,z} = z^2 \sigma_{m,p}$. Therefore, Eq. 45 can be rewritten as

$$D = q_F \, z \, \sigma_{m,p} \cdot 10^{11} \tag{46}$$

The dose rate $\frac{dD}{dt}$ in rads/sec can be found by substituting the beam current density i_F in amperes/cm^2 for the charge density q_F collected on the Faraday cup, and

$$\frac{dD}{dt} = \frac{i_F}{z} \sigma_{m,z} \cdot 10^{11} = i_F z \sigma_{m,p} \cdot 10^{11}. \tag{47}$$

¶ By comparing the charge Q_F collected on the Faraday cup with the charge Q_I collected in an ionization chamber that is sensitive over the entire area of the beam, one can obtain directly the specific ionization p (in ion pairs per cm) for the particular beam used and for the particular gas in the ionization chamber. If n is the number of particles that pass through the ionization chamber with electrode spacing d cm, we have

$$Q_I = n \, d \, p \, \frac{e}{c} \cdot 10 = n \, d \, p \, 1.602 \cdot 10^{-19} \tag{48}$$

where the factor $\frac{e}{c} \cdot 10$ is the charge per ion pair in coulombs. If the same number of particles n is collected in the Faraday cup, Eqs. 41 and 48 give

$$\frac{Q_I}{Q_F} = \frac{pd}{z}, \text{ or } p = \frac{z}{d} \frac{Q_I}{Q_F} \tag{49}$$

Simultaneous measurements of Q_I and Q_F provide a means of determining W, the energy per ion pair formed in the ionization-chamber gas, in case its value is not exactly known (see Section II-C), or a means of determining σ_m in case the energy of the particles is not known. Since the specific ionization p is related to the energy loss of the particle, $\frac{dE}{dx}$, by

$$p = \frac{1}{W}\frac{dE}{dx} = \frac{\rho_g \sigma_m}{W}, \tag{50}$$

where ρ_g is the density of the gas, and σ_m is the mass stopping power of the gas, Eq. 49 can be rewritten as

$$\frac{Q_I}{Q_F} = \frac{d\,\rho_g \sigma_m}{z\,W} \tag{51}$$

Hence a measurement of the ratio Q_I/Q_F gives the ratio σ_m/W. If the stopping power of the incident particles is known, the value of W for the particular beam used and for the particular gas in the ionization chamber can be determined from this ratio. (See Sections II-A and II-B for curves of the stopping power as a function of proton energy.) In case the stopping power of the beam is not known, one can use the measured ratio Q_I/Q_F with a given value of W to determine the stopping power of the ionization-chamber gas. (See Section II-C for a discussion of the measured values of W.)

The quantity important in biological measurements is the stopping power (LET) of tissue rather than the stopping power of the gas. The mass stopping power of tissue can be obtained by multiplying the mass stopping power of the gas by the relative mass stopping power of the two materials (Section II-B). As an example of the magnitude of quantities involved, the ratio Q_I/Q_F is approximately 140 for 300-Mev protons passing through a 1/2-inch ionization chamber filled with nitrogen.

3. Sources of Error

Various experimental errors may occur in Faraday-cup measurements. The following precautions should be taken in order to minimize these errors (1, 21).

a. The absorbing block must not only be long enough to stop the primary beam, but it must also stop charged secondaries that may be produced in nuclear interactions.

b. The block must be wider than the diameter of the beam so that particles are not scattered out of the sides of the block. As the range of the particles increases, the lateral spread of the beam from scattering also increases. For example, tests by Aamodt et al. (1) showed that for 340-Mev protons the radius of the block should be at least 1-1/2 inches greater than the radius of the beam.

c. The distance between the absorbing block and the window should be small to minimize the loss of particles scattered by the window. For the same reason external absorbers should be placed as close as possible to the Faraday cup.

d. Secondary electrons emitted from any of the surfaces traversed by the beam should be prevented from entering or leaving the collection block. Both high- and low-energy secondaries may be produced. A magnetic field of approximately 100 gauss oriented perpendicular to the direction of the beam is sufficient to cause low-energy secondary electrons to return to the surfaces from which they are emitted. A test for the effects of low-energy secondary electrons may be made by observing the current collected by the Faraday cup as a function of positive or negative voltage applied to a wire screen or thin foil placed between the window and the collection block. A correction of several per cent may still have to be made for high-energy electrons knocked out of the window (21).

e. To prevent formation of ions in the residual gas surrounding the collection block the pressure in the vacuum chamber should not exceed 10^{-4} mm Hg.

f. Since the currents to be measured are small, the leakage resistance of the Faraday cup and accompanying circuits should be correspondingly high. The insulators should not be exposed to the direct beam, since they may become conductors in the presence of radiation.

C. Particle Counters

For the measurement of low-intensity beams, individual particles may be counted with instruments such as ionization chambers, proportional counters, or scintillation counters. This method is particularly useful for determining the range and straggling, and hence the energy and energy distribution, of the particles (Section II-F and II-G). Combined with ionization-chamber measurements, counter measurements can be used to determine the rate of energy loss or LET of the particles. In most applications, however, counters cannot be used for direct dosimetry because of the very high counting rates obtained even from low-intensity beams. From the number of particles in the beam, the dose and related quantities can be calculated by means of the equations in Section III-B-2.

D. Activation Dosimetry

High-velocity particles produce radioactive isotopes as a result of their interactions with atomic nuclei. The resulting radioactivity may be used as an independent method of measuring dose, particularly to check on the accuracy of more readily available techniques and to give information about dose distributions. Since almost every element becomes radioactive when bombarded with high-energy particles, a large number of variations of this technique are possible.

1. The decay curve

The constituents of soft tissue are principally hydrogen (10%), carbon (12%), oxygen (73%), and nitrogen (4%) (47). Inspection of the tables of radioactive isotopes (36) indicates that the highest activities that will be observed in tissue a few minutes after exposure are those of C^{11} (20.5-min half life), N^{13} (10-min half life), and O^{15} (2-min half life). These isotopes all emit low-energy positrons, which are stopped by a few millimeters of aluminum, and the resulting annihilation gamma rays can be counted conveniently in a scintillation counter (3). A typical tissue-activation curve produced by 190-Mev deuterons is shown in Fig. 16. The final slope of the curve agrees closely with the 20.5-min half life of C^{11}, while the contributions from N^{13} and O^{15} are evident in the initial part of the curve. For many measurements it is more convenient to activate pieces of polyethylene $(CH_2)_n$ or polystyrene $(CH)_n$, since the only appreciable activity induced in them is that of C^{11} and the decay curve is a single exponential curve.

2. Dose calculations

Depending on the geometry used during exposure, activation dosimetry can be used to determine the total flux F of particles/sec in the beam or it can be used to determine the flux density f (particles/cm^2-sec) over a small area. For measuring the total flux F the sample must extend over the entire area of the beam, but when the flux density f is to be determined the sample should intercept only a small fraction of the beam. We shall consider the second case, but the basic relationships are similar in the two cases.

If $\mathfrak{N}$ atoms of an element with nuclear cross section σ_n cm^2 are irradiated by a constant flux density of f particles/cm^2-sec, and the decay constant of the radioactive produce is λ sec^{-1} ($\lambda = 0.69315/T_{1/2}$, where $T_{1/2}$ is the half life), the rate of formation of radioactive atoms from a single reaction follows the differential equation,

$$\frac{dn}{dt} = f\,\sigma_n\,\eta - \lambda_\eta\,, \tag{52}$$

where n is the number of radioactive atoms at any time t during bombardment. The total activity induced depends on both the intensity and the duration of exposure. After the end of bombardment the disintegration rate R is governed by the usual law of radioactive decay,

$$R = -\frac{dn}{dt} = \lambda n = \lambda n_{t=0}\, e^{-\lambda t}\,. \tag{53}$$

From Eqs. 52 and 53, the number R of disintegrations per sec at any time t after the end of bombardment is

$$R = f\,\sigma_n\,\eta\,(1 - e^{-\lambda\tau})\,e^{-\lambda t}\,, \tag{54}$$

where τ is the duration of the bombardment in seconds. By use of the approximation,

$$1 - e^{-\lambda\tau} \approx \lambda\tau\, e^{-\frac{\lambda\tau}{2}}\,, \tag{55}$$

Eq. 54 can be simplified to the form

$$R \approx \lambda f\tau\,\sigma_n\,\eta\, e^{-\lambda(t+\frac{\tau}{2})}\,. \tag{56}$$

or

$$f\tau \approx \frac{R}{\lambda\,\sigma_n\,\eta}\, e^{\lambda(t+\frac{\tau}{2})}\,. \tag{57}$$

The dose D in rads (see Eqs. 44 and 45) can then be calculated from the equation

$$D = 1.602\cdot 10^{-8}\,\sigma_m\, f\,\tau\,, \tag{58}$$

where σ_m is the mass stopping power of the sample in Mev $gm^{-1}\,cm^2$, to be distinguished from the nuclear cross section σ_n. The term $f\,\tau$ is usually evaluated by extrapolating the 20.5-minute half-life portion of the disintegration curve back to the middle of bombardment time when $t = -\frac{\tau}{2}$.

To obtain the dose from activation measurements, one must know the nuclear cross section σ_n for each transmutation that can produce a particular radioactive isotope. Since cross-section measurements are usually

made for elements in their naturally occuring isotopic abundance, the summation over $\sigma_n \mathfrak{N}$ need only be made over all contributing elements. The number of atoms $\mathfrak{N}$ of one element in the sample is given by

$$\mathfrak{N} = \frac{N_o}{A} a \mathfrak{M}, \tag{59}$$

where N_o is Avogadro's number, $\mathfrak{M}$ is the mass of the sample, a is the percent by weight of the element being considered, and A is the atomic weight of the element. [illegible] Figure 17 shows the cross sections determined by Crandall et al. (21) for the formation of C^{11} as a function of the energy of protons and deuterons incident on carbon. As an example of the magnitude of activities obtained with 300-Mev protons, a dose of 1000 rad/min is delivered to tissue by a flux density of $1.75 \cdot 10^{10}$ protons/cm^2-min. This corresponds to a beam-current density (Eq. 47) of $4.68 \cdot 10^{11}$ amp/cm^2. The activation of carbon for one minute with this flux density produces C^{11} with an initial activity of 1070 disintegrations/min per mg of carbon irradiated.

3. Applications

In practice it is difficult to make an accurate absolute determination of beam-flux density from measurements of induced radioactivity. First, the efficiency of the counter for the particular sample must be known in order to obtain the absolute disintegration rate of the sample, and any determination is subject to the usual errors in sample counting. Second, an initially monoenergetic beam will contain neutrons and low-energy scattered protons after passing through absorbing material. These secondary particles may make a substantial contribution to the induced activity, especially when the cross section rises with decreasing energy as with protons incident on carbon (Fig. 17). Third, the determination depends on the accuracy with which the cross section is known.

Activation dosimetry is most useful as a check on other methods of dose measurement and for determining the beam profile. If two samples of masses $\mathfrak{M}_1$ and $\mathfrak{M}_2$ are irradiated for the same length of time at constant particle-flux densities f_1 and f_2, the ratio of the two disintegration rates R_1 and R_2 is, from Eq. 54,

$$\frac{R_1}{R_2} = \frac{f_1 \mathfrak{M}_1 e^{-\lambda t_1}}{f_2 \mathfrak{M}_2 e^{-\lambda t_2}}, \tag{60}$$

where the samples are counted at times t_1 and t_2 respectively. Hence, by exposing a mosaic of small pieces of material and counting them with a counter of fixed (but not necessarily known) efficiency, a map of relative beam flux density can be obtained.

Activation dosimetry is a convenient method for checking the calibration of an ionization chamber as a function of dose rate. A typical determination of saturation error in an ionization chamber is shown in Fig. 14, where both activation and Faraday-cup determinations are plotted (63).

When partial-body irradiation of animals is performed, the activity induced in a tissue sample can give a direct measure of the corrections that must be applied to the dose measurement. Care must be taken, however, since activity induced in vivo in tissue can be transported by the exchange of water and CO_2. This effect is probably small. In irradiation of the pituitary gland of rats with 190-Mev deuterons, Tobias et al. (75) compared the activity induced in the pituitaries of sacrificed animals when the entire head was irradiated with that induced by a narrow beam aligned with the center of the gland. They found that the dose received by the gland from the narrow beam was approximately two-thirds of that received when the whole head was irradiated. The difference was attributed to divergence of the beam, to scattering, and to imperfect alignment of the pituitary gland with the beam.

E. Photographic Film

The principles of photographic film dosimetry have been reviewed by Dudley in Chapter 7. For proton energies above 10 Mev, photographic film forms a convenient instrument for dose measurement, and it has distinct advantages in some applications. For low-energy particles, whose range is not much greater than the thickness of the emulsion, photographic dosimetry requires tedious analysis of individual tracks in special nuclear track emulsions, and the method is limited to special applications such as measuring particle fluxes over areas of only a few square microns (90).

Tochilin et al (78) measured the response of several different films to beams of protons, deuterons, and alpha particles ranging in energy from 0 to 380 Mev. They found that the optical density produced in Kodak NTB emulsion was roughly proportional to the dose or energy transfer, whereas the densities produced in Eastman Translite and Type 5302 are more nearly proportional to particle flux density. Different films also show a large variation in absolute sensitivity.

There are many factors that influence the response of a film as a function of exposure. Aside from the properties inherent in the particular emulsion used, the energy of the incident particles, the conditions under which the film is processed, the length of time between exposure and processing, the thickness of the emulsion, and the type of densitometer used to read the film all affect the over-all sensitivity. Therefore it is essential that the film be calibrated under conditions identical with those used for the experimental determinations. For calibration purposes a series of known exposures should be made over the entire range of doses used. These exposures can be monitored by other instruments, such an an ionization chamber or a Faraday cup. The beam used for calibrating the film--in particular, the energy distribution--should be as nearly as possible identical with the beam used in the unknown exposures. Furthermore, the calibration film should be from the same emulsion batch and should be processed with the other films. Finally, all the films should be scanned with the same photoelectric densitometer. By use of the curve of percent transmission or optical density as a function of exposure that is obtained from the calibration film, the dose at any point in the other films can be determined with good accuracy. For a further discussion of sources of error and care in technique, the reader is referred to Chapter 7, Section II-A.

Probably the most important application of film dosimetry lies in the mapping of complicated radiation fields. The photographic technique has the advantages that a series of films can be inserted into a tissuelike phantom without distorting the radiation field appreciably, and that excellent resolution can be obtained by using a small scanning aperture in the densitometer. There is the additional advantage that a large amount of information can be obtained with a relatively short beam exposure. The method is especially valuable in rotation therapy (33), where the radiation field continually changes as the target is rotated. Figure 18 shows isodose curves obtained by Welch (85) for irradiation of the human pituitary with 340-Mev protons (76). The measurements were made on a series of Eastman Kodak Super panchro-press films exposed between thin sheets of black bakelite and held in a lucite phantom that represented the patient's head. The phantom was aligned in the beam and rotated $\pm 30^{\circ}$ about a horizontal axis during exposure. Nine exposures were superimposed, each one taken at a different orientation of the phantom about a vertical axis. In this way the film exposure corresponded to the complete treatment schedule of the patient. Densities measured on the films were

converted to dose by comparison with calibration exposures made on another film without rotation.

F. Crystal Detectors

Various semiconducting crystals are known to change their electrical conductivity when exposed to ionizing radiations (30, 81). Welch and Tobias have used this property in CdS crystals to measure the dose distribution within a narrow beam of 190-Mev deuterons (75, 86). They obtained direct currents of several microamps from a crystal less than 1 mm^3 in volume. Difficulties were encountered, however, because the crystals responded with a time lag of several minutes, and their sensitivity depended on previous exposure to radiation. The work of Jacobs with pulsed x-rays beams (39) indicates that these difficulties may be overcome in the future by measuring the alternating-current component produced in the crystals by pulsed beams.

IV. Applications

Several applications of heavy-particle beams in radiological and radiobiological research are listed below.

A. Radiation Physics and Chemistry of Solid, Liquid, and Gaseous Systems

Heavy particles are of interest in this field because the changes produced by them are often quantitatively and qualitatively different from those produced by x-rays, γ-rays, or electrons. The decomposition of water has been studied by Toulis using protons, deuterons, and alpha particles (79, 80), while Garrison and associates have used heavy particles to study radiation-induced synthesis and decomposition of simple organic molecules in aqueous systems (31). In this work the beam was allowed to stop in an aqueous sample after penetrating a thin glass window, and the vessel containing the sample was used as a Faraday cup (83).

Heavy particles are important in studying radiation damage to solids. Yockey et al. developed a refrigerated target assembly for such studies (89). Heavy particles have also been used for introducing lattice imperfections into semiconducting crystals (65).

B. Molecular Biophysics

Pollard and the Yale University Biophysics group have pioneered in adapting cyclotron-accelerated particles to biophysical studies of large molecules (56, 57, 29, 38, 66). Following the early observations and theories by Dessauer, Svedberg, and others (56) they have developed methods for measuring the cross section and shape of certain biologically active molecules such as enzymes and phage particles in a dehydrated state. In some instances the estimation of the "cross section" of biologically active prosthetic groups has proven feasible and the method may be adapted to measuring the thickness of molecular layers. In each of these measurements the particles impinge on a target which is part of the absorbing block of a Faraday cup. The depth of penetration of the beam is controlled by the use of absorbers.

C. Studies of Biological Effectiveness

For many years it has been known that heavy particles often exhibit greater effectiveness in some of their biological actions than light ones (92). Complete evaluation of these effects, and determination of the Relative Biological Effectiveness (RBE) as a function of Lineal Energy Transfer (LET), is not only practically important but has aided in the determination of the site

of action of radiations in the living cell. Successful theories of the biological action of radiation must account for the dependence of RBE on LET. Microorganisms and tissue membranes (e.g. cornea) are particularly well suited to studies where a relatively uniform and high LET is required throughout the sample (91, 61, 62, 56, 82, 32, 23). This type of sample is usually irradiated in air, and ionization chambers are used for dosimetry.

The presence of very heavily ionizing nuclei in primary cosmic radiation raises the problem of their biological action in connection with possible space flight. Studies with particle accelerators may yield practical knowledge in this connection (10, 73).

D. Microirradiation Studies

Zirkle and Bloom have demonstrated the feasibility of irradiating very small regions within individual cells with protons (90). The proton beam is obtained from a 2-Mev Van de Graaff machine by collimation with specially made microapertures. In order to measure the dose it is necessary to count with a Geiger-Muller or proportional counter the individual particles that pass through the aperture. Since scattering occurs at the edges of the aperture, the actual distribution of particle trajectories is measured by exposing a nuclear track plate to the microbeam and counting individual proton tracks. In the relatively short period since microbeams of protons and ultraviolet rays have been available, many interesting new facts have been learned with regard to the physical mechanisms of cell division, particularly the nature of chromosome attachments and the role of the spindle in division, and new radiation-induced cellular abnormalities have been observed.

E. Physiological Studies with Localized Radiation+

In 1946 Wilson (88) suggested that protons in the 100-Mev region could be used to produce lesions in definite volume elements of animal tissue. The great penetration, definite range, and relatively small scattering of high-energy protons make these particles more suitable for localized irradiation studies than many other available radiations. Taking advantage of the Bragg ionization peak and the rotational exposure technique permits much greater depth dose than surface dose. This method has been applied successfully to problems in animal radiobiology which require deep exact localization of the radiation. Deep therapy of animal tumors has been attempted (72), and a study has been made of the site of cataract formation in rabbits by localizing

the beam in different parts of the lens of the rabbit eye (82). It has also been possible to irradiate selectively the pituitary gland of animals and to produce states resembling surgical hypophysectomy (75). Small brain lesions approximately 1 mm^3 in volume have been produced which may be helpful in the difficult task of unraveling the physiological functions of various loci of the central nervous system (59). In studies of this kind one should know the isodose surfaces in tissue, and LET of the particles, as well as the total dose delivered.

In discussing the biological applications of heavy particles, one finds active work in at least five different fields of radiation biology. In each of these fields the use of heavy particles is leading to new results and the extension of knowledge. It is possible that heavy-particle beams may become an accepted form of radiation therapy within a few years. The dosimetry of heavy-particle beams is sufficiently well established so that some routine investigations can be carried out with relative ease. Many details remain to be investigated.

BIBLIOGRAPHY

1. Aamodt, R. L., Peterson, V., and Phillips, R., UCRL-1400 (1951).
2. Allison, S. K., and Warshaw, S. D., Revs. Mod. Phys. 25, 779 (1953).
3. Anger, H. O., Rev. Sci. Instru. 22, 912 (1951).
4. Anger, H. O. and Tobias, C. A., unpublished data.
5. Aron, W. A., Hoffman, B. G., and Williams, F. C., "Range-Energy Curves" AECU-663, Technical Information Service, Oak Ridge, Tenn. (1951).
6. Barber, W. C., Phys. Rev. 97, 1071 (1955).
7. Bernier, J. P., Johns, H. E., and Cormack, D. V., Radiation Research 3, 213 (1955).
8. Bethe, H. A., and Ashkin, J., in "Experimental Nuclear Physics", p. 166, Vol. 1 (E. Segrè, Ed.), Wiley and Sons, Inc. (1953).
9. Binks, W., Acta Radiologica, Suppl. 117, 85 (1954).
10. Birge, A. C., J. Aviation Med. 25, 326 (1954).
11. Birge, A. C. and Sayeg, J. A. unpublished data.
12. Blatt, J. M. and Weisskopf, V. F., "Theoretical Nuclear Physics", Wiley and Sons, New York (1952).
13. Bloembergen, N. and van Heerden, P. J., Phys. Rev. 83, 561 (1951).
14. Boag, J. W., Brit. J. Rad. 23, 601 (1950).
15. Boag, J. W., Brit. J. Rad. 25, 649 (1952).
16. Boag, J. W. and Wilson, T., Brit. J. of Appl. Phys. 3, 222 (1952).
17. Brown, S. C., Nucleonics 2, No. 6, 10 (1948).
18. Caldwell, D. O., Phys. Rev. 88, 131 (1952).
19. Cook, L. J. McMillan, E. M., Peterson, J. M. and Sewell, D. C., Phys. Rev. 75, 7 (1949).
20. Coor, T., Hill, D. A., Hornyak, W. F., Smith, L. W., and Snow, G., Phys. Rev., 98, 1369 (1955).
21. Crandall, W. E., Millburn, G. P., Pyle, R. V., and Birnbaum, W., UCRL-2756 Rev. (1955). Phys. Rev., in press.
22. de Carvalho, H. G. and Yagoda, H., Phys. Rev. 88, 273 (1952).
23. Ehrenberg, L., and Andersson, G., Nature 173, 1086 (1954).
24. Ellis, R. H., Jr., Rev. Sci. Inst. 25, 336 (1954).
25. Ellis, R. H., Jr., Rossi, H. H., and Failla, G., Phys. Rev. 97, 1043 (1955).
26. Eyges, L., Phys. Rev. 74, 1534 (1948).
27. Farr, L. E., Robertson, J. S., and Stickley, E., Proc. Natl. Acad. Sci. U. S. 40, 1087 (1954).

28. Fermi, E., "Nuclear Physics". Notes by Orear, J., Rosenfeld, A. H., and Schluter, R. A., Univ. of Chicago Press (1950).

29. Fluke, D. J. and Pollard, E. C., Ann. New York Aca. Sci. 59, 484 (1955).

30. Frerichs, R., Phys. Rev. 72, 594 (1947).

31. Garrison, W. M., Haymond, H. R., and Weeks, B. M., Rad. Res. 1, 97 (1954).

32. Giles, N. H., and Tobias, C. A., Science 120, 993 (1954).

33. Granke, R. C., Wright, K. A., Evans, W. W., Nelson, J. E., and Trump, J. G., Am. J. Roentgenol. Radium Therapy Nuclear Med. 72, 302 (1954).

34. Gray, L. H., Proc. Camb. Phil. Soc. 40, 92 (1944).

35. Healey, R. H., and Reed, J. W., "The Behaviour of Slow Electrons in Gases." Amalgamated Wireless Limited, Sydney (1941).

36. Hollander, J. M., Perlman, I., and Seaborg, G. T., Rev. Mod. Phys., 25, 469 (1953).

37. Holloway, M. G., and Livingston, M. S., Phys. Rev. 54, 18 (1938).

38. Hutchinson, F., Ann. New York Acad. Sci. 59, 494 (1955).

39. Jacobs, J. E., Electrical Engineering 70, 667 (1951).

40. Jaffé, G., Ann. d. Physik 42, 303 (1913).

41. Jesse, W. P., Forstat, H., and Sadauskis, J., Phys. Rev. 77, 782 (1950).

42. Jesse, W. P. and Sadauskis, J., Phys. Rev. 88, 417 (1952).

43. Jesse, W. P., and Sadauskis, J., Phys. Rev. 90, 1120 (1953).

44. Jesse, W. P., Rad. Res. Soc. Meeting, New York, May, 1955.

45. Jesse, W. P., and Sadauskis, J., Phys. Rev. 97, 1668 (1955).

46. Kruger, P. G., Rad. Res. 3, 1 (1955).

47. Lea, D. E., "Actions of Radiations on Living Cells", Macmillan Co., New York (1947).

48. Lewis, M. N., Private communication.

49. Lindhard, J., and Scharff, M., Kgl. Danske Videnskab. Selsk. Mat.-fsy. Medd. 27, No. 15 (1953).

50. Loeb, L. B., "Basic Processes of Gaseous Electronics." University of California Press, Chapter 6 (1955).

51. McManus, H., Sharp, W. T., and Gellman, H., Phys. Rev. 93, 924 (1954); and Private communication.

52. Mather, R., and Segrè, E., Phys. Rev. 84, 191 (1951).

53. Millburn, G. P., Birnbaum, W., Crandall, W. E., and Schecter, L., Phys. Rev. 95, 1268 (1954).

54. Ovadia, J., Danzker, M., Beattie, J. W., and Laughlin, J. S., Radiation Research 3, 340 (1955).

55. Platzman, R. L., in "Symposium on Radiobiology," (J. J. Nickson, Ed.), p. 97, Wiley and Sons, Inc. (1952).

56. Pollard, E., in "Advances in Biological and Medical Physics" (J. H. Lawrence and C. A. Tobias, Eds.), Vol. 3, Academic Press, New York (1953).

57. Pollard, E., Ann. New York Acad. Sci. 59, 469 (1955).

58. Rich, M., and Madey, R., UCRL-2301 (1954).

59. Roberts, J. E., Garcia, J. F., Henry, J. P., Anderson, O. K., Anger, H. O., and Tobias, C. A., Private communication.

60. Rossi, B., "High Energy Particles." Prentice-Hall, New York (1952).

61. Sayeg, J. A., and Birge, A. C., Rad. Res. 1, 560 (1954).

62. Sayeg, J. A., UCRL-2293 (Thesis, University of California, 1954).

63. Sayeg, J. A., and Tobias, C. A., unpublished data.

64. Schaefer, H. J., "The Radial Spread of the Tissue Ionization Dosage in Heavy Nuclei Tracks of the Primary Cosmic Radiation." U. S. Naval School of Aviation Medicine, Report No. NM 001 059.13.04 (1952).

65. Seitz, F., Rev. Mod. Phys. 26, 7 (1954).

66. Setlow, R., Ann. New York Acad. Sci. 59, 471 (1955).

67. Simons, D. G., J. Aviation Med. 25, 380 (1954).

68. Smith, J. H., Phys. Rev. 71, 32 (1947).

69. Symon, K. R., Thesis, Harvard University (1948).

70. Thompson, T. J., UCRL-1910 (Thesis, University of California, Berkeley, 1952).

71. Tobias, C. A., Weymouth, P. P., Wasserman, L. R., and Stapleton, G. E., Science 107, 115 (1948).

72. Tobias, C. A., Anger, H. O., and Lawrence, J. H., Am. J. Roentgen. and Rad. Therapy 67, 1 (1952).

73. Tobias, C. A., J. Aviation Med. 23, 345 (1952).

74. Tobias, C. A., Phys. Rev. 85, 764 (1952).

75. Tobias, C. A., Van Dyke, D. C., Simpson, M. E., Anger, H. O., Huff, R. L., and Koneff, A. A., Am. J. Roentgen. Rad. Therapy and Nuc. Med. 72, 1 (1954).

76. Tobias, C. A., Roberts, J. E., Lawrence, J. H., Low-Beer, B. V. A., Anger, H. O., Born, J. L., McCombs, R., and Huggins, C., UCRL-3035 (1955).

77. Tobias, C. A., and Anger, H. O., unpublished data.

78. Tochilin, E., Shumway, B. W., and Kohler, G. D., Radiation Research, to be published; Radiology 66, Abstract in press.

79. Toulis, W. J., UCRL-1332 (1951).

80. Toulis, W. J., UCRL-583 (1950).

81. van Heerden, P. J., and Milatz, J. M. W., Physica 16, 517 (1950).

82. von Sallmann, L., Tobias, C. A., Anger, H. O., Welch, G., Kimura, S. F., Munoz, C. M., and Drungis, A., Arch. Ophthalmology 54, 489 (1955).

83. Weeks, B. M., UCRL-3071, in preparation.

84. Weiss, J., and Bernstein, W., Phys. Rev. 98, 1828 (1955).

85. Welch, G. P., Appendix B, UCRL-3035 (1955). (cf. Ref. 76.)

86. Welch, G. P., private communication.

87. Wilkinson, D. H., "Ionization Chambers and Counters," Cambridge University Press (1950).

88. Wilson, R. R., Radiology 47, 487 (1946).

89. Yockey, H. P., Andrew, A., Fillmore, F. L., Glasgow, L. E., Hunt C. d'A., and Pepper, J. H., Rev. Sci. Instru. 25, 1011 (1954).

90. Zirkle, R. E., and Bloom, W., Science 117, 487 (1953).

91. Zirkle, R. E., and Tobias, C. A., Arch. Biochem. and Biophys. 47, 282 (1953).

92. Zirkle, R. E., "Radiation Biology" (A. Hollaender, Ed.), Vol. I, Part 1, p. 315, McGraw Hill, New York (1954).

FIGURE CAPTIONS

Fig. 1. Theoretical curves for the mass stopping power of protons in water (58), nitrogen (5), aluminum (68), and argon (5), as a function of proton energy.

Fig. 2. The relative mass stopping power of tissue compared with nitrogen as a function of proton energy.

Fig. 3. The value of W for air, nitrogen, and argon as a function of the energy of protons and α-particles. (34, 45) The value of W plotted is instantaneous, not integrated to the end of the particle range.

Fig. 4. Theoretical range-energy curves for protons of 0 to 14 Mev in water (58), nitrogen (5), aluminum (68), and argon (5).

Fig. 5. Theoretical range-energy curves for protons of 10 to 200 Mev in water, nitrogen, aluminum, and argon.

Fig. 6. Theoretical range-energy curves for protons of 100 to 4000 Mev in water, nitrogen, aluminum, and argon.

Fig. 7. Typical Bragg curve and number-distance curve for 190-Mev deuterons in aluminum (72).

Fig. 8. Experimental arrangement for measuring the Bragg curve.

Fig. 9. Typical set of isodose surfaces for a 190-Mev deuteron beam of circular cross section stopped in lucite. The number on each curve gives the dose relative to the surface dose.

Fig. 10. Perspective view of an ionization chamber with electrostatic collection field parallel to the beam direction. The ionization chamber has been cut in half.

Fig. 11. Perspective view of an ionization chamber with electrostatic collection field perpendicular to the beam direction.

Fig. 12. Block diagram of ionization chamber, integrating electrometer and high voltage supply.

Fig. 13. Typical saturation curves for 190-Mev deuterons in air and nitrogen. The beam was pulsed 68 times per second. Separation of the high voltage and collection electrodes was 1/2 inch.

Fig. 14. Dependence of error on dose rate in a parallel-plate ionization chamber exposed to 190-Mev deuterons of 68 pulses/sec and approximately 1 μsec pulse length. The ionization chamber contained nitrogen and used 2 000 volts

FIGURE CAPTIONS (CONT.)

collection voltage with 1/2 inch separation of the electrodes. The determination of error was made by comparing the ionization current with the current measured by a Faraday cup and with the C^{11} activity induced in polyethylene discs.

Fig. 15. Perspective view of a Faraday cup which is cut in half.

Fig. 16. Typical decay curve for activity induced in tissue by 190-Mev deuterons (courtesy of B. Lowenhaupt). Counter efficiency approximately 20%.

Fig. 17. Cross section for the formation of C^{11} by protons and deuterons incident on carbon as a function of particle energy (21).

Fig. 18. Isodose curves obtained for a horizontal beam of 340-Mev protons by photographic film dosimetry. The series of films was exposed in a lucite phantom that was rotated about a horozontal axis. Nine exposures, taken at different orientations of the phantom about a vertical axis, were superimposed.

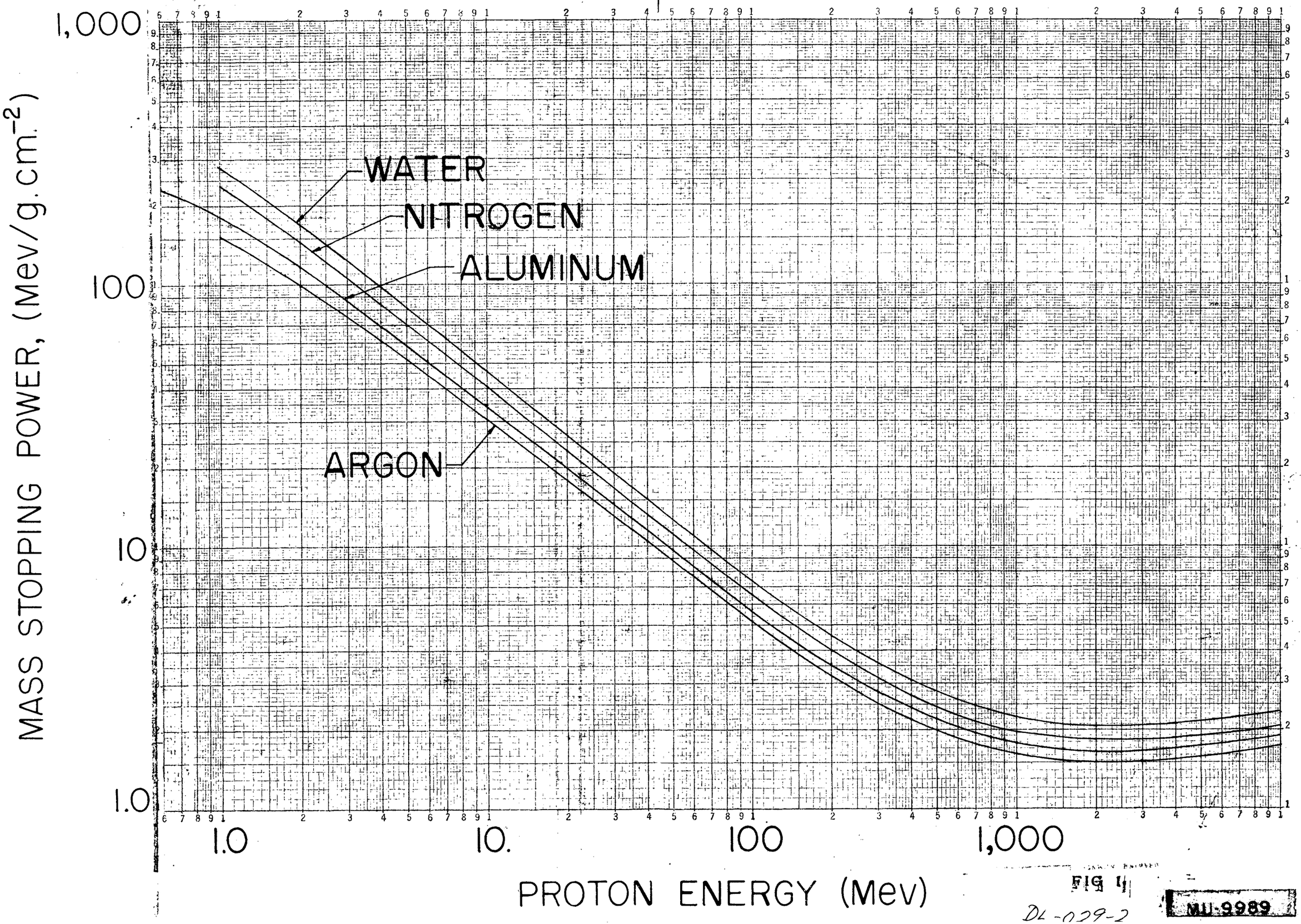

FIG 1

DL-029-2

MU-9989

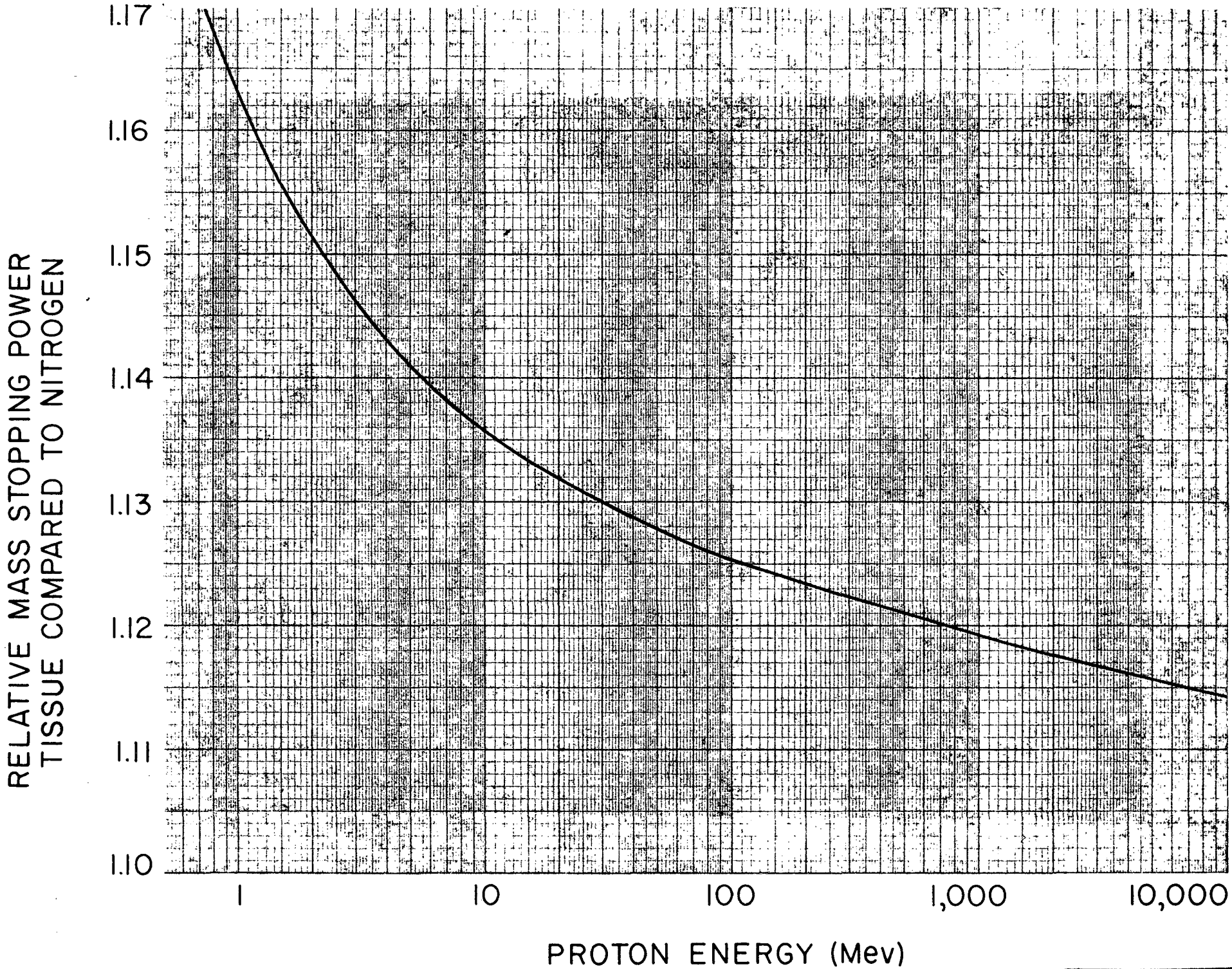

FIG 2

[redacted]

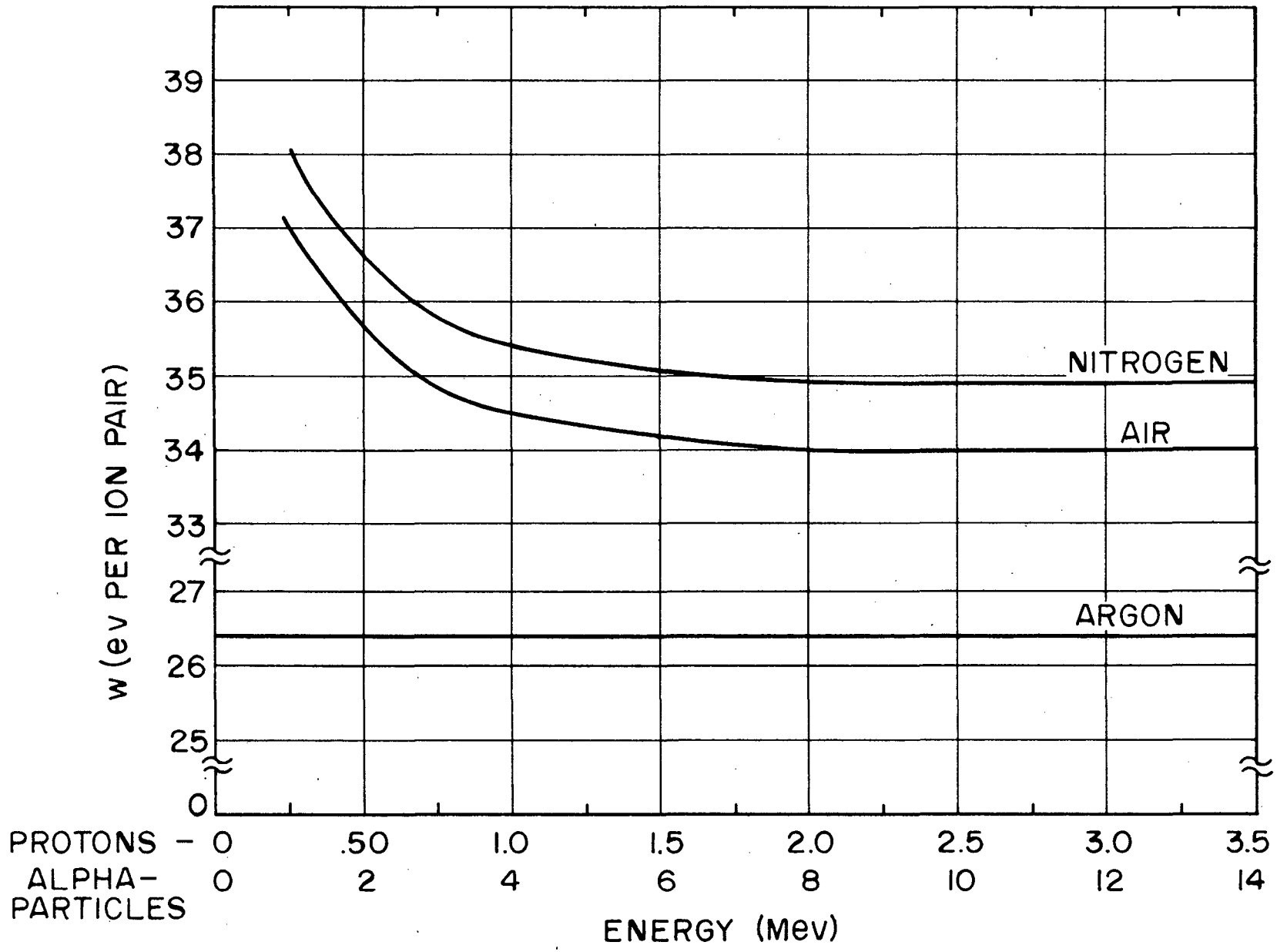
39
38
37
36
35
34
33
27
26
25
0
W (ev PER ION PAIR)
NITROGEN
AIR
ARGON
PROTONS - 0 .50 1.0 1.5 2.0 2.5 3.0 3.5
ALPHA-PARTICLES 0 2 4 6 8 10 12 14
ENERGY (Mev)

MU-9998

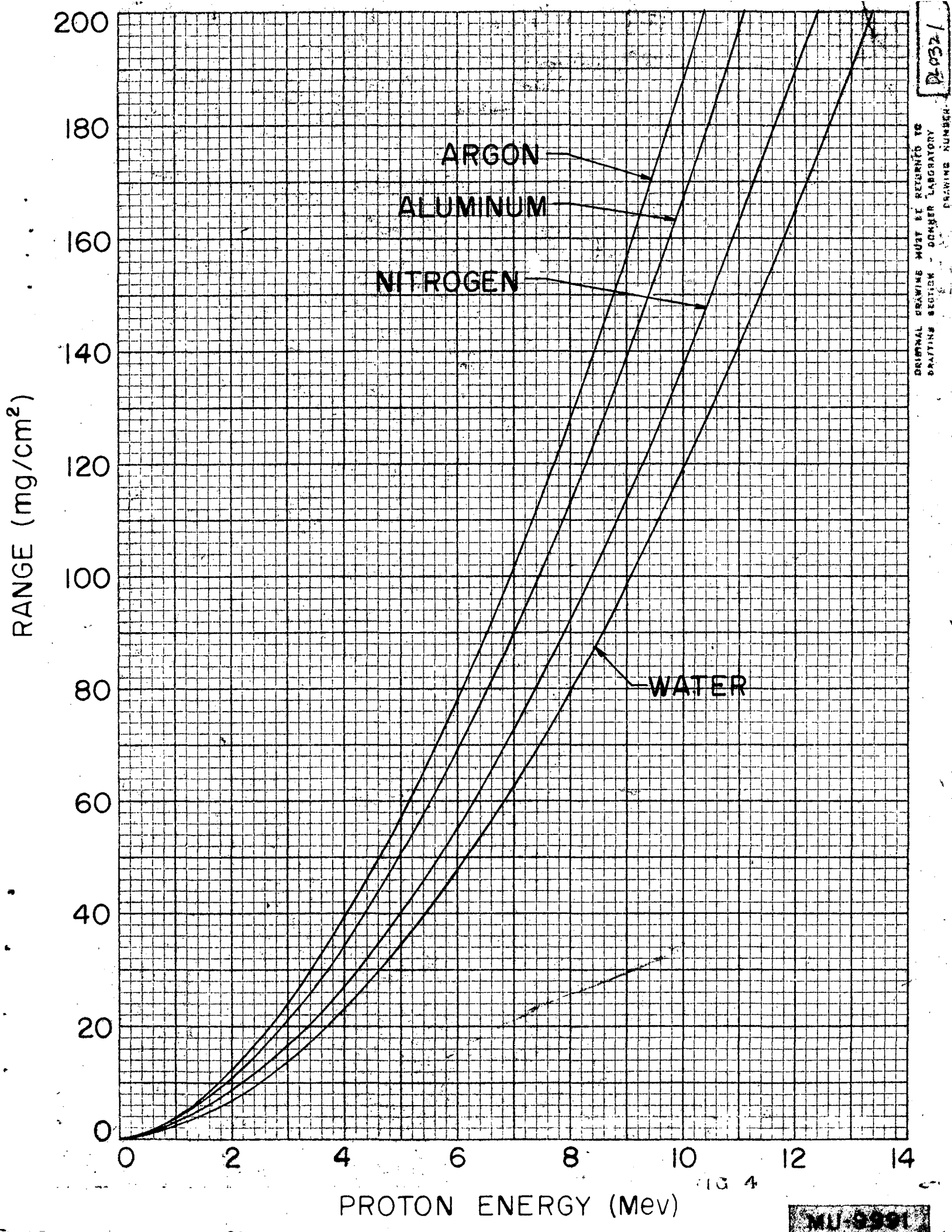
200
180
160
140
120
100
80
60
40
20
0
RANGE (mg/cm²)
ARGON
ALUMINUM
NITROGEN
WATER
0
2
4
6
8
10
12
14
PROTON ENERGY (Mev)
D-032
ORIGINAL DRAWING MUST BE RETURNED TO
DRAFTING SECTION - DOWNER LABORATORY
DRAWING NUMBER
MU-9991

FIG 4

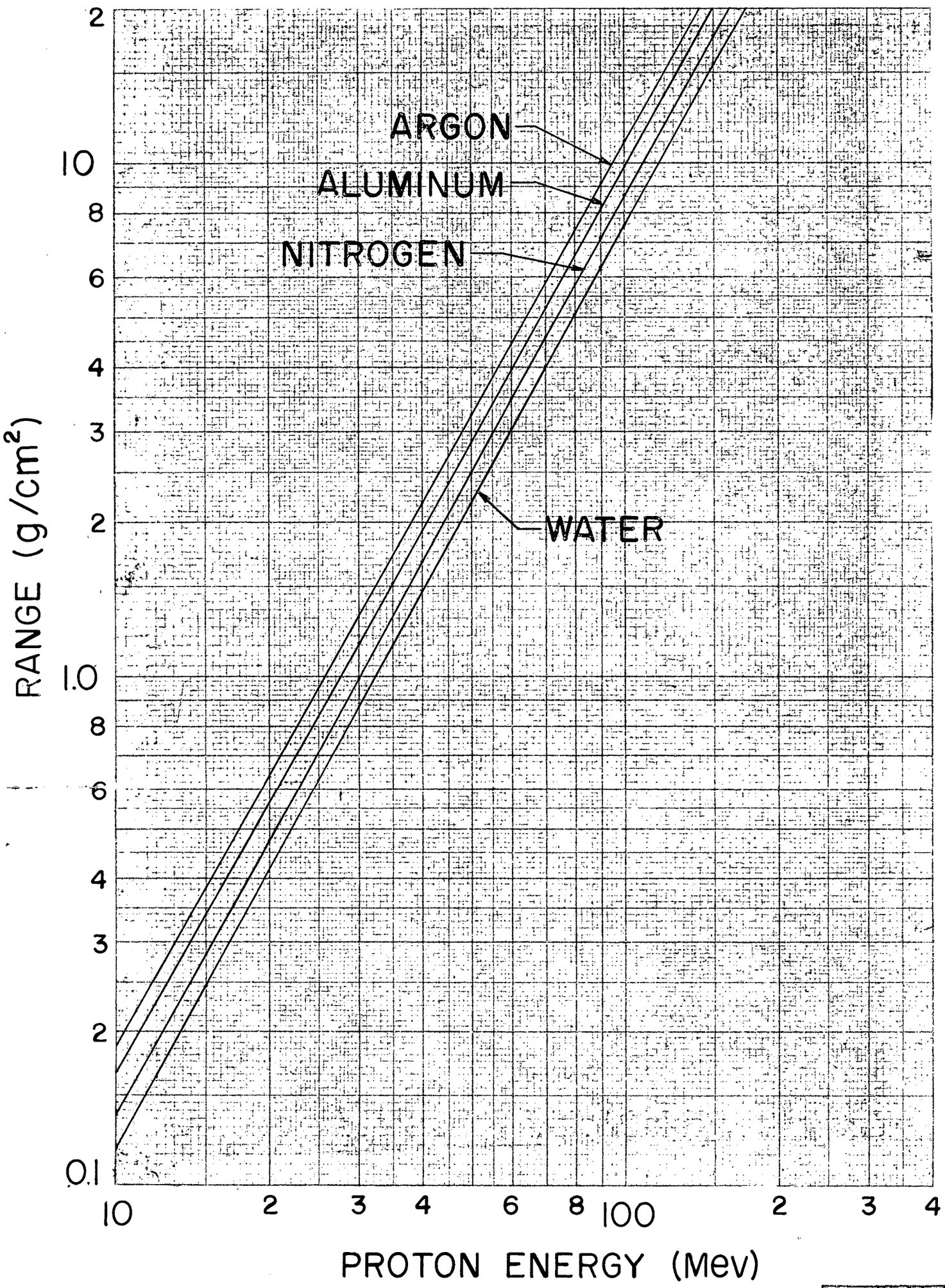
ARGON
ALUMINUM
NITROGEN
WATER
RANGE (g/cm²)
2
10
8
6
4
3
2
1.0
8
6
4
3
2
0.1
10
2
3
4
6
8
100
2
3
4
PROTON ENERGY (Mev)

MU-9992

FIG 5

FIG 6

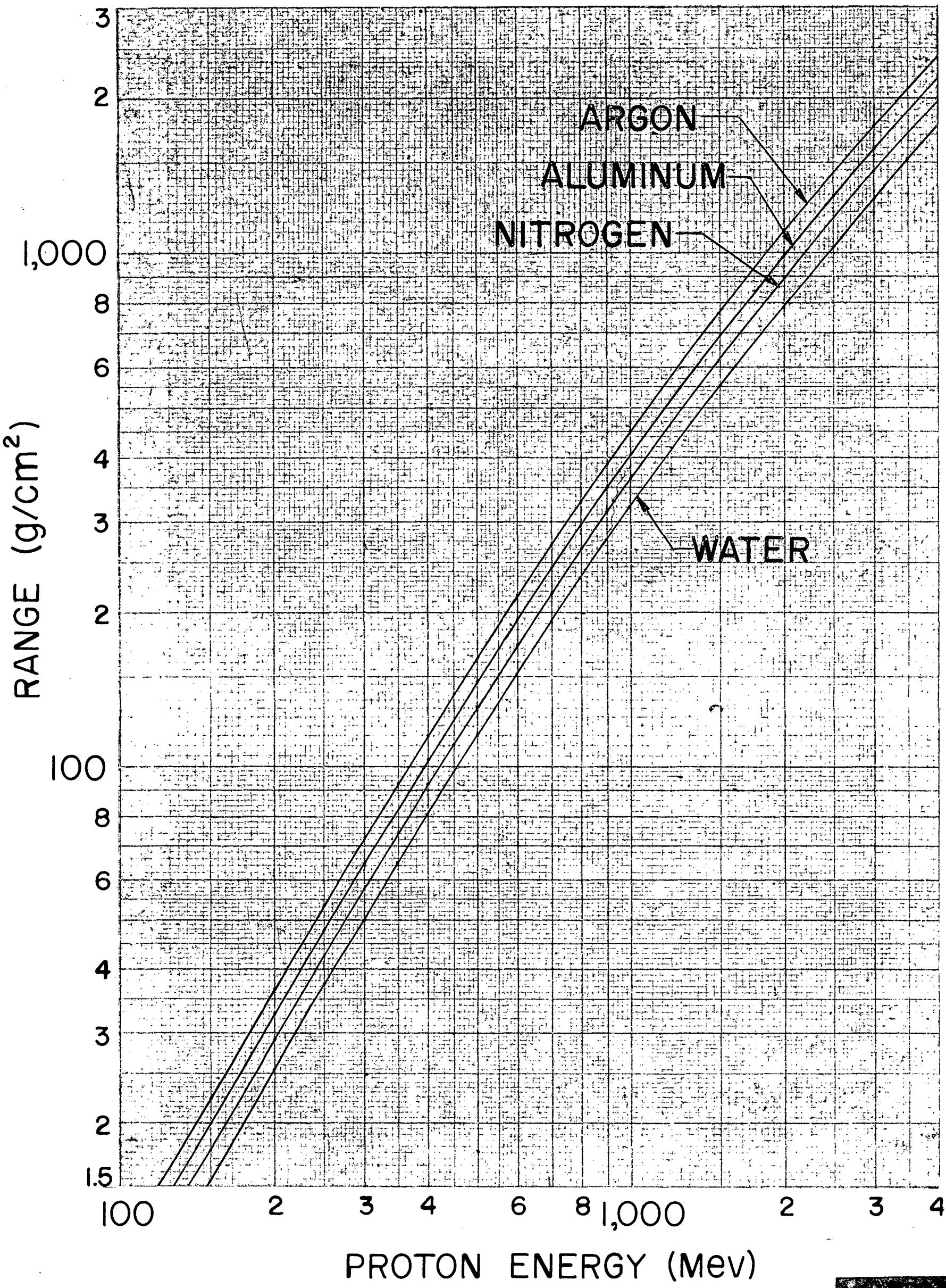

[redacted]

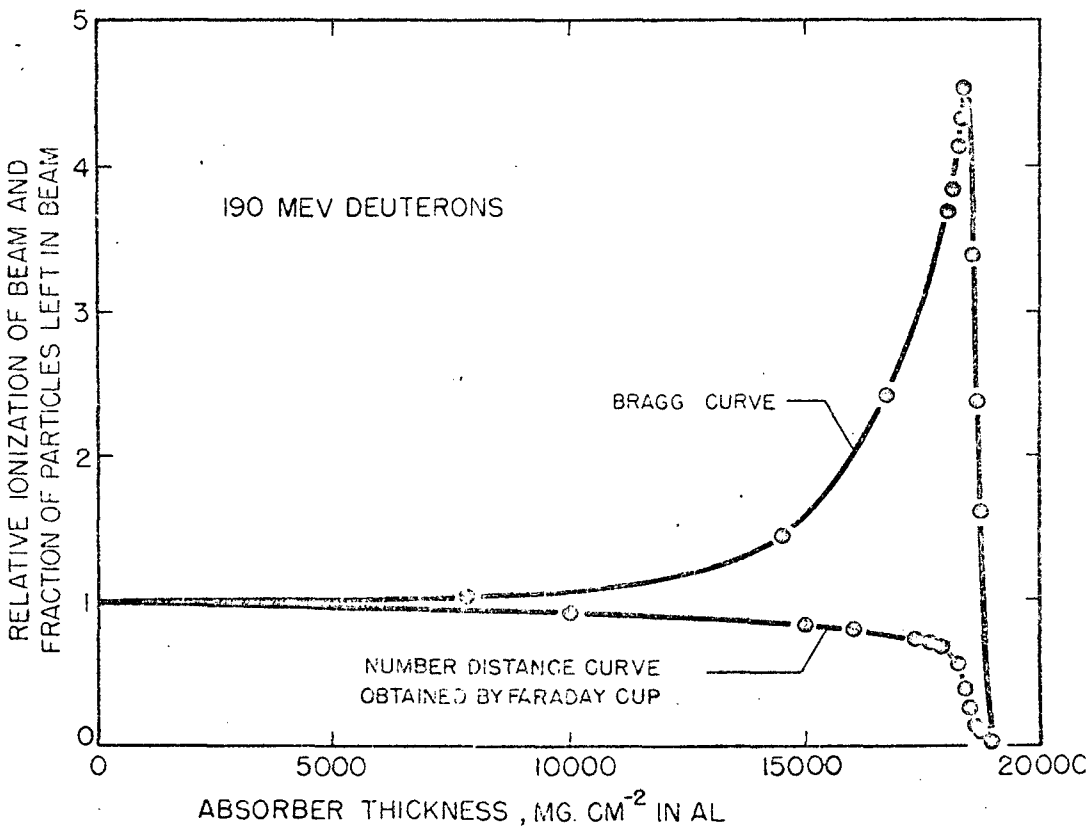
190 MEV DEUTERONS
BRAGG CURVE
NUMBER DISTANCE CURVE
OBTAINED BY FARADAY CUP
RELATIVE IONIZATION OF BEAM AND
FRACTION OF PARTICLES LEFT IN BEAM
ABSORBER THICKNESS , MG. CM^{-2} IN AL
0
1
2
3
4
5
0
5000
10000
15000
20000

Fig. 7

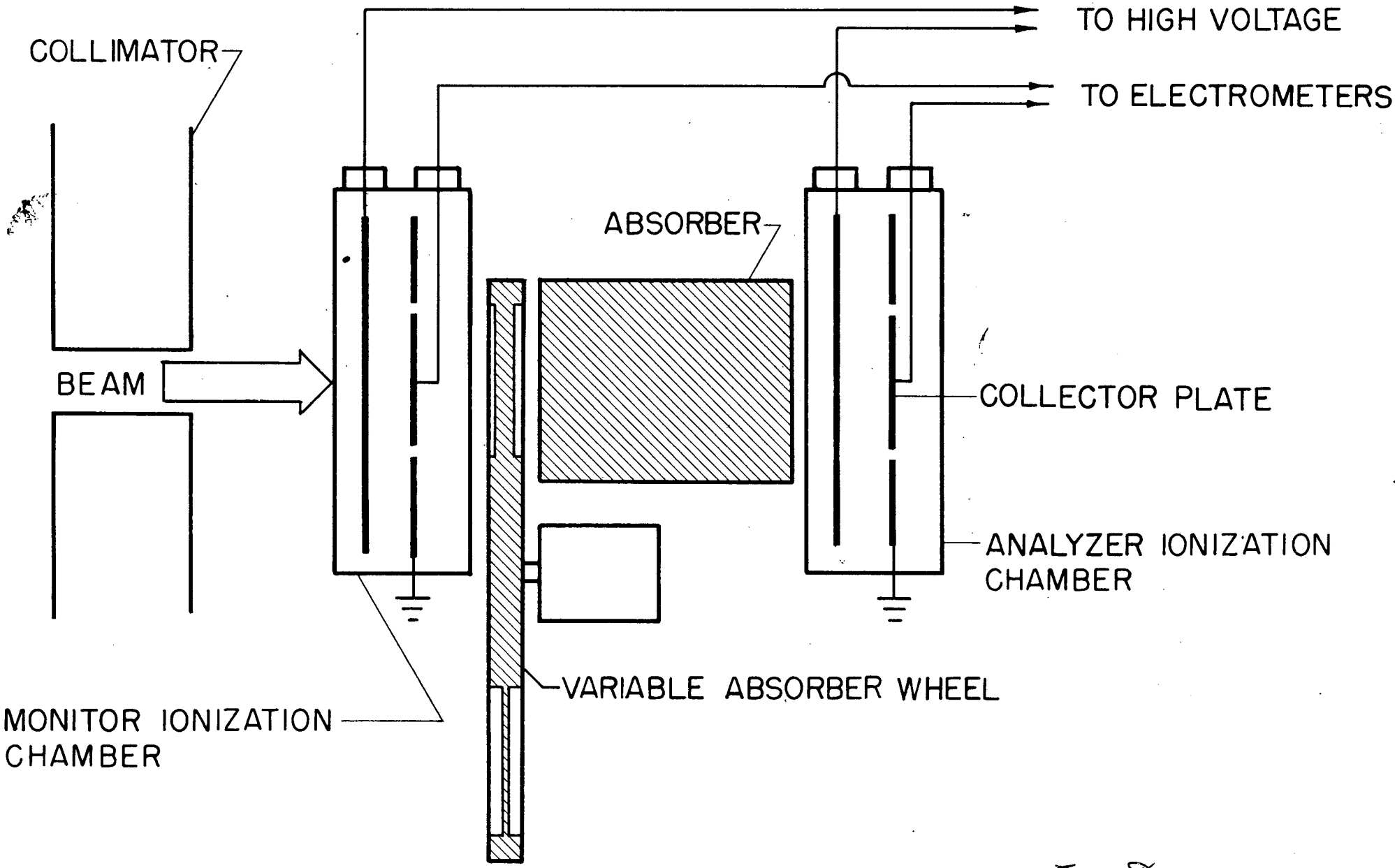
TO HIGH VOLTAGE
TO ELECTROMETERS
COLLIMATOR
ABSORBER
BEAM
COLLECTOR PLATE
ANALYZER IONIZATION CHAMBER
VARIABLE ABSORBER WHEEL
MONITOR IONIZATION CHAMBER

Fig 8

GN9021

190 MEV DEUTERON BEAM
LUCITE ABSORBING MATERIAL
2.54 cm COLLIMATOR

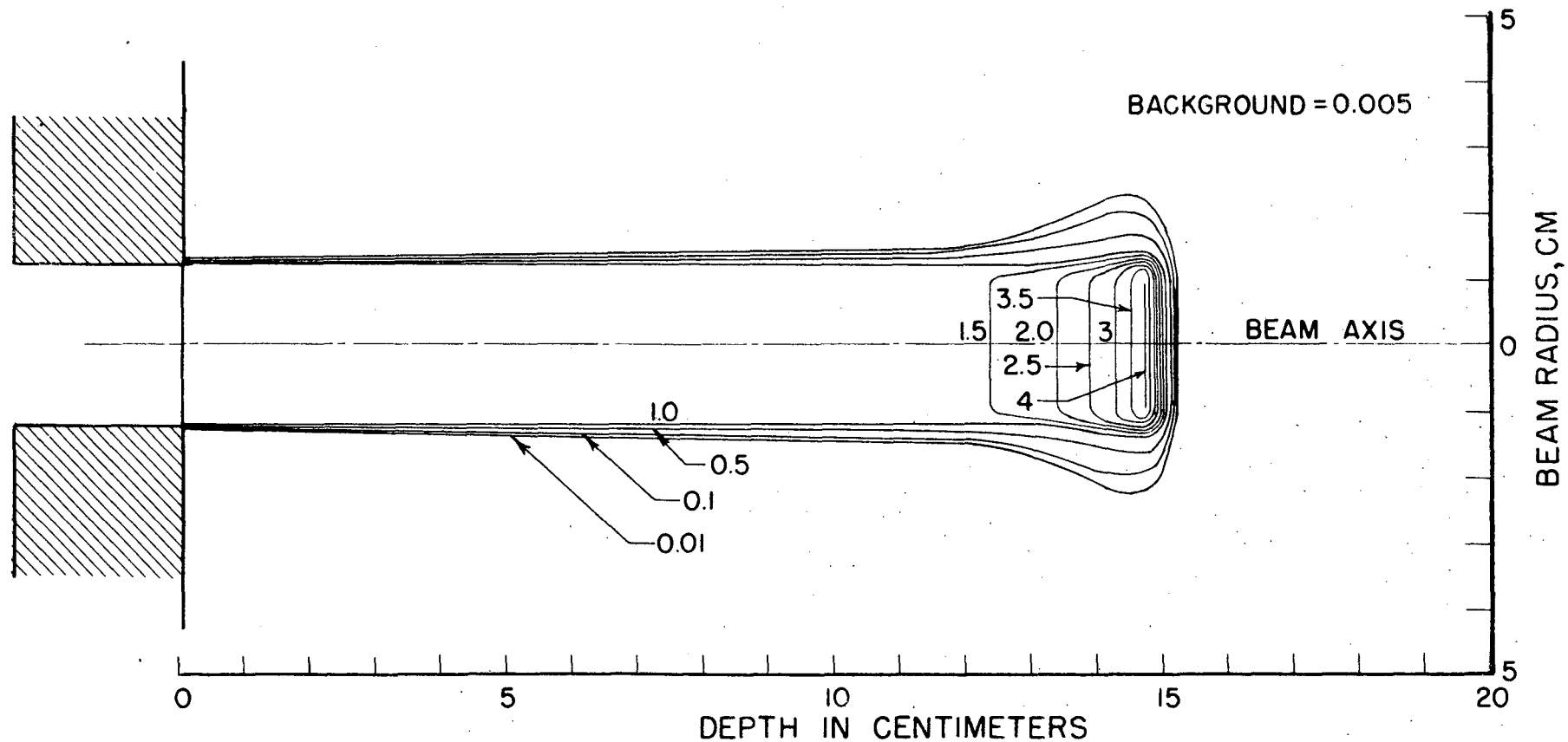

FIG 9

5K-200-1

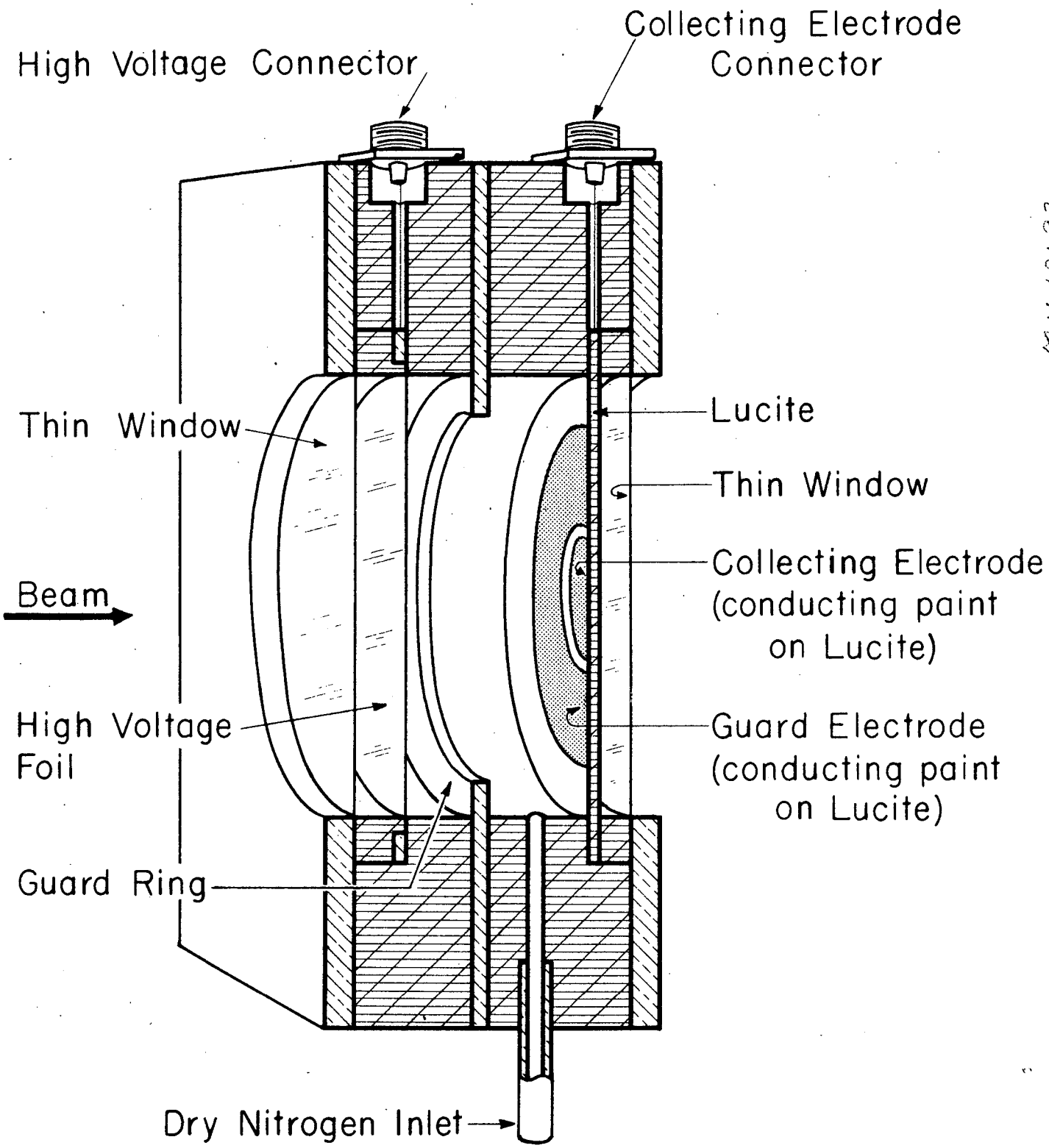

FIG 10

6N9411

MU 10193

3/5 of 6

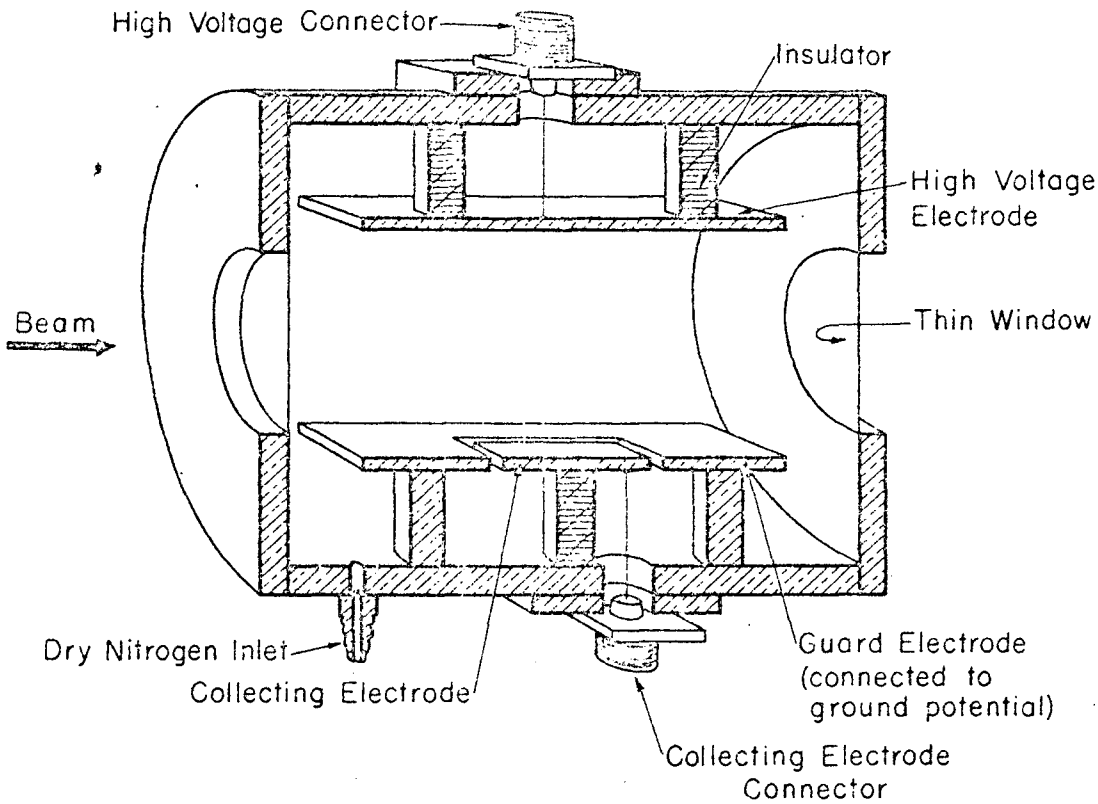
High Voltage Connector
Insulator
High Voltage Electrode
Beam
Thin Window
Dry Nitrogen Inlet
Collecting Electrode
Guard Electrode (connected to ground potential)
Collecting Electrode Connector

Fig. 11

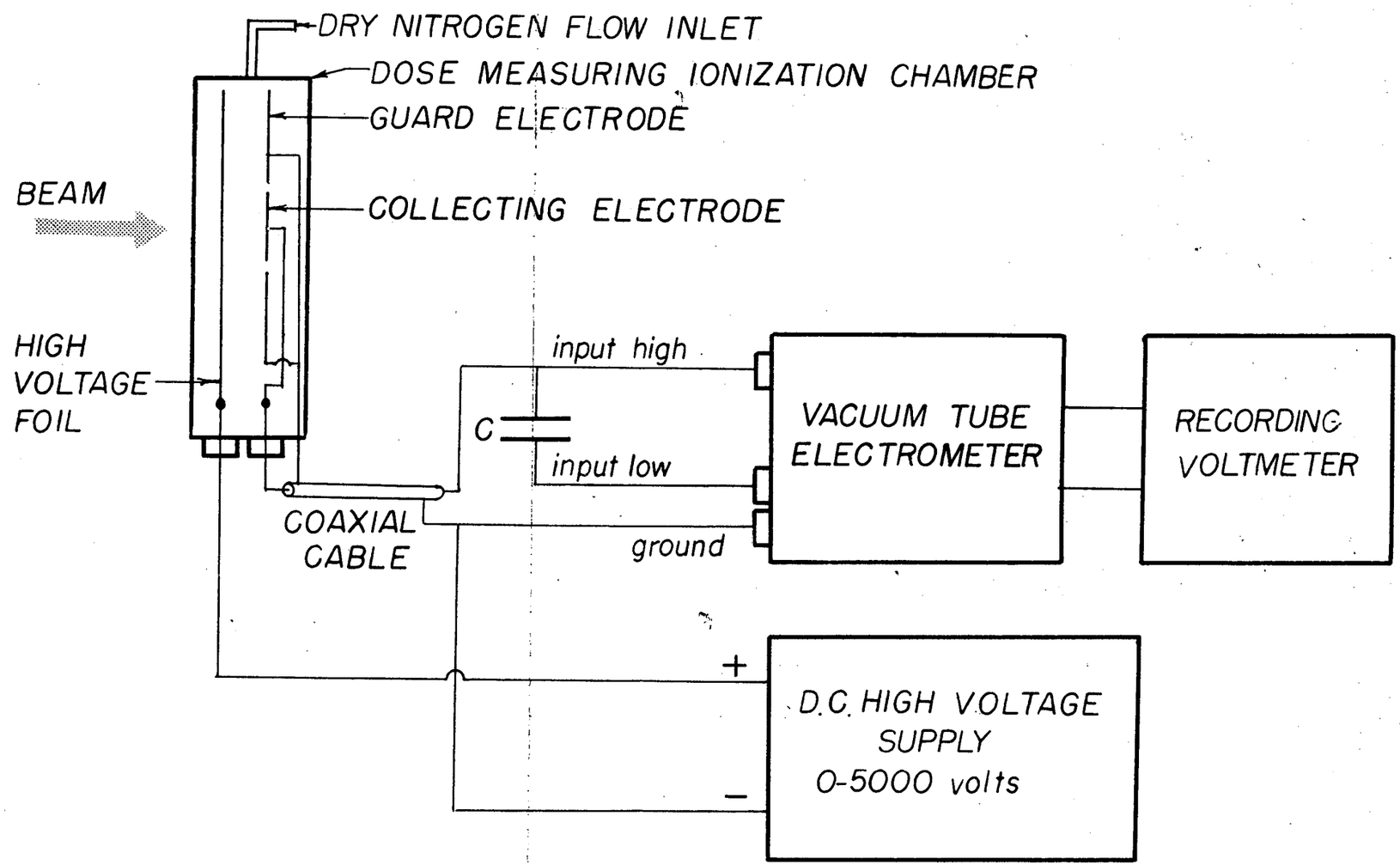

[redacted]

FIG 12

HM HONG 6N8682
7-1-55

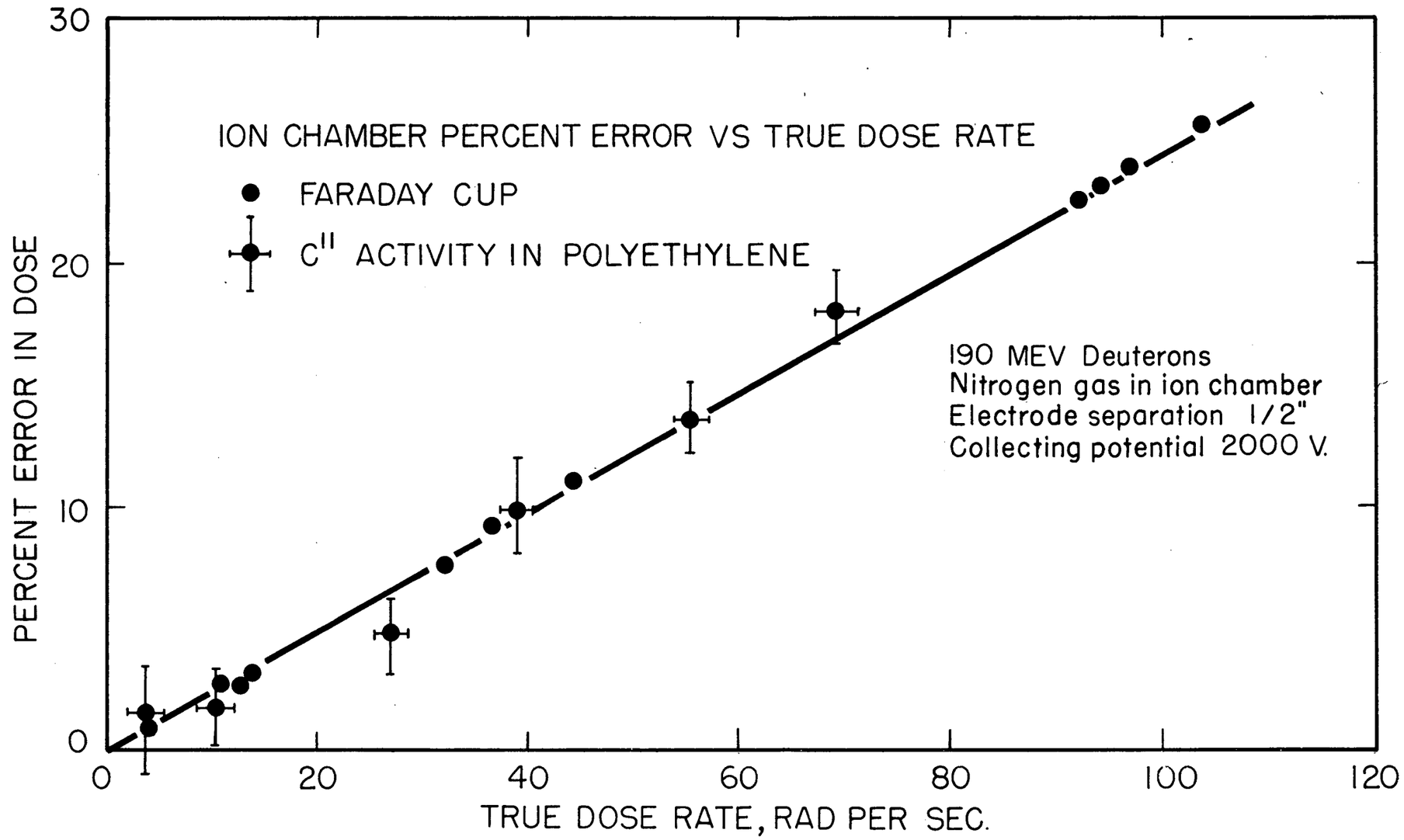

FIG 14

8-20-55 H.M.HONG

6N3052

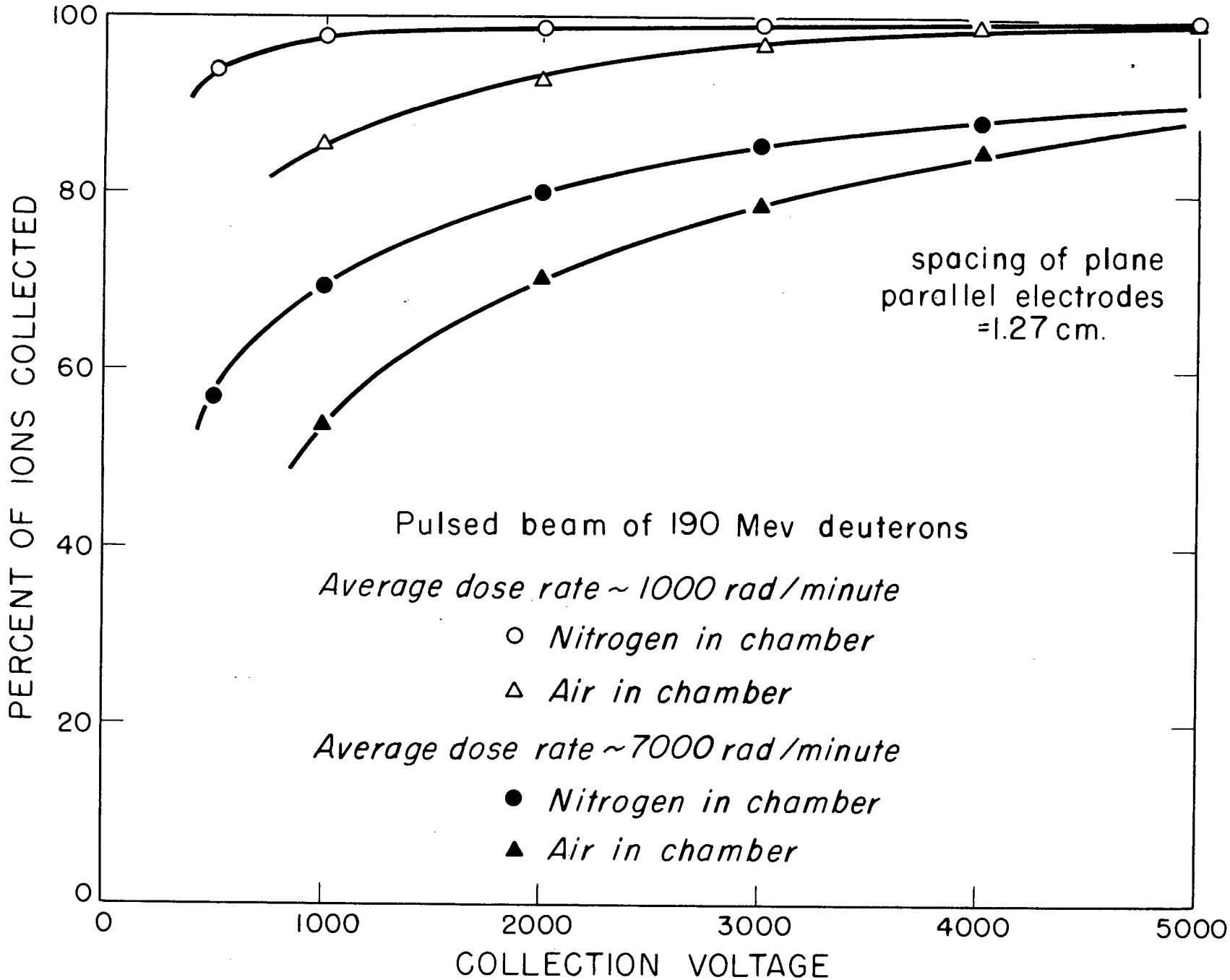

Fig. 13

6N930-1

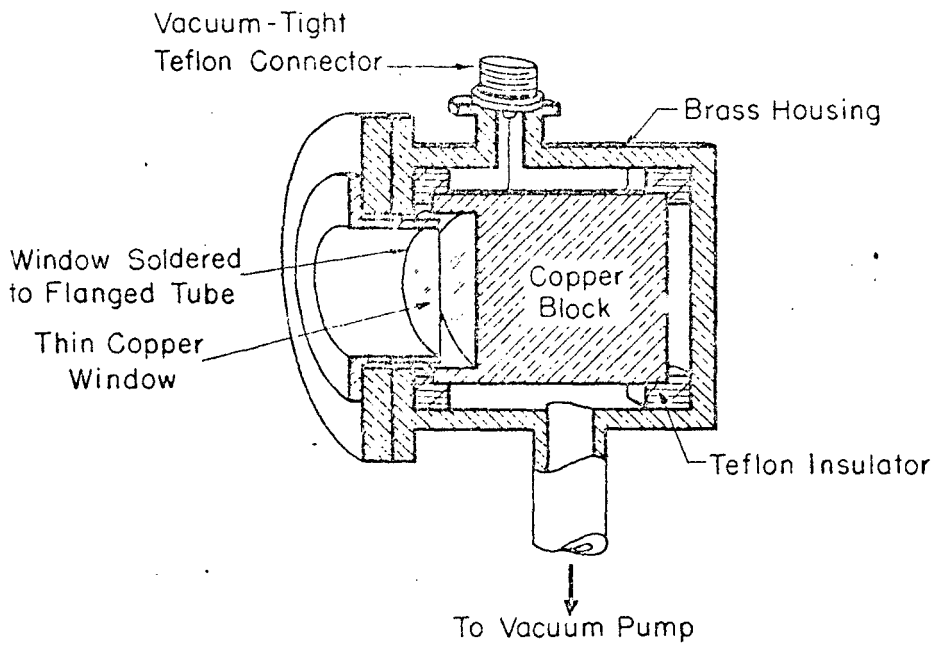
Vacuum-Tight
Teflon Connector
Brass Housing
Window Soldered
to Flanged Tube
Copper
Block
Thin Copper
Window
Teflon Insulator
To Vacuum Pump

Fig. 15

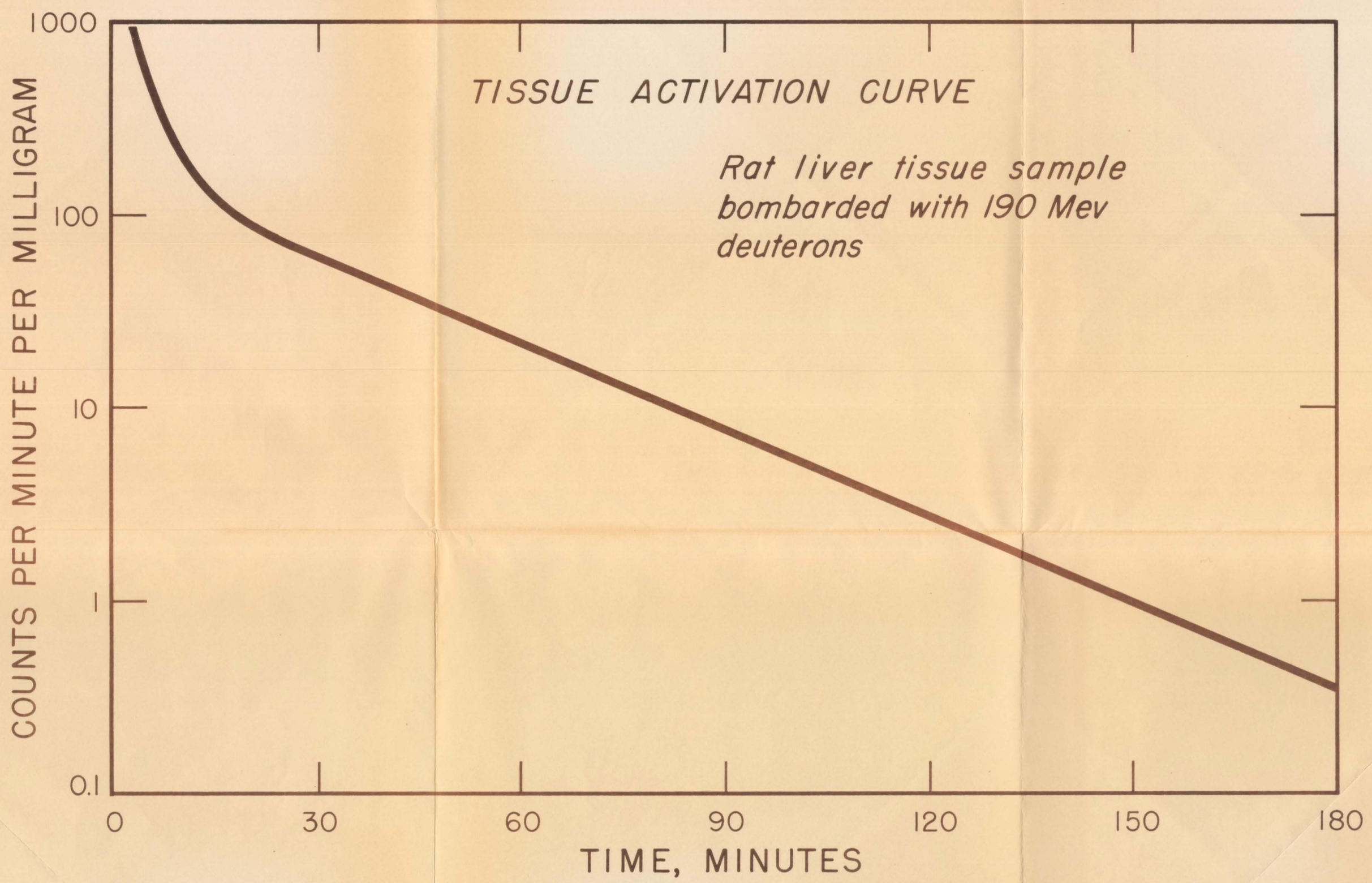

FIG 16

6N931-3

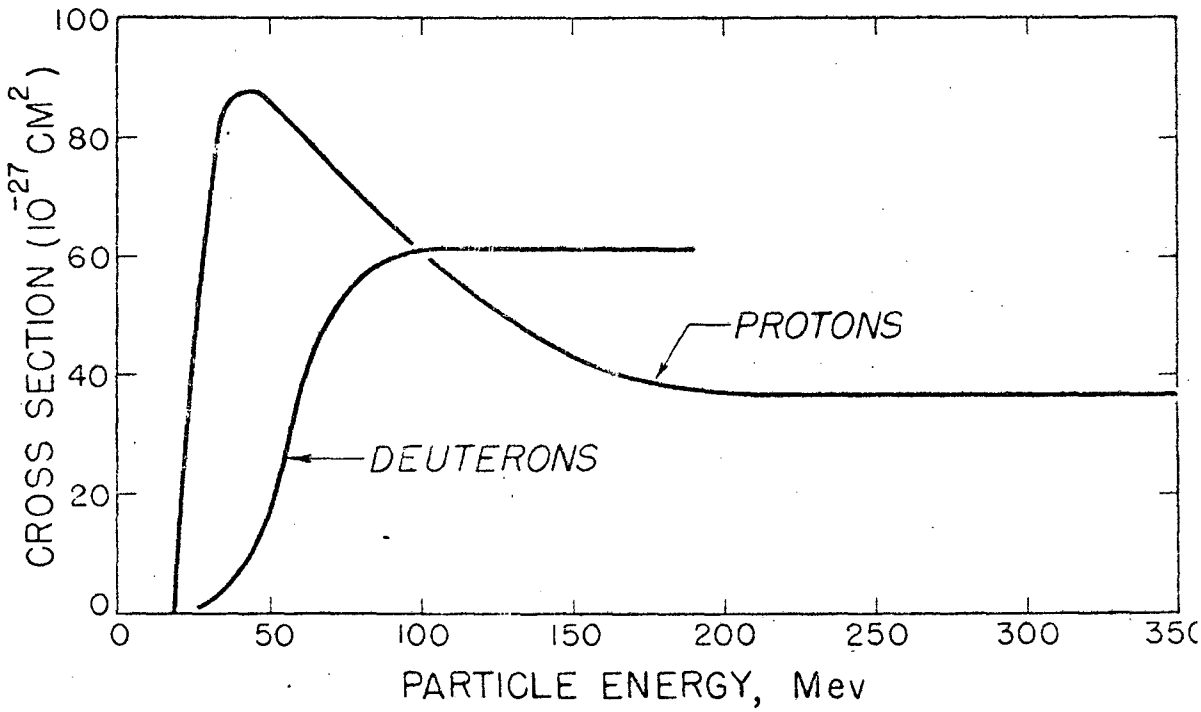
100
80
60
40
20
0
CROSS SECTION (10^{-27} CM^2)
0
50
100
150
200
250
300
350
PARTICLE ENERGY, Mev
PROTONS
DEUTERONS

Fig. 17

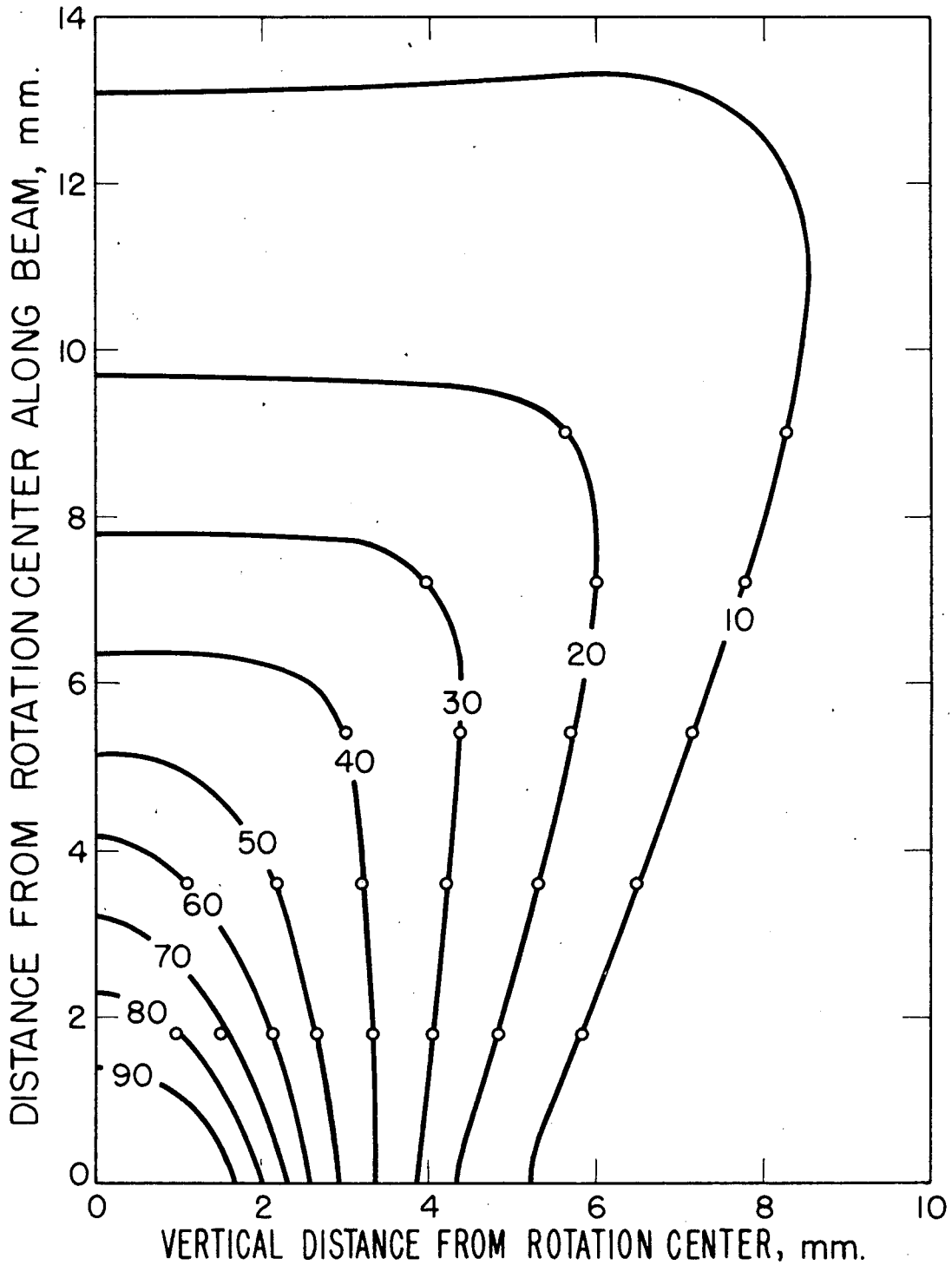

FIG 18

6N-887-1